國立臺灣大學理學院海洋研究所

碩士論文

Graduate Institute of Oceanography

College of Sciences

National Taiwan University

Master Thesis

結合北太平洋海溫模態與熱帶地區海洋熱含量探討 ENSO 的演變

The Linkages Between Victoria Mode and Tropical Ocean Heat Content on ENSO Evolution

林廷恩

Ting-En Lin

指導教授：曾于恒 博士

Advisor: Yu-Heng Tseng, Ph.D.

中華民國 109 年 3 月

March 2020

doi:10.6342/NTU202000712

中文摘要

先前的研究指出考慮熱帶地區次表層海洋熱含量的暖水體 (例如：Warm water volume，簡稱 WWV) 以及北太平洋中緯度地區海平面氣壓變異所引起的海溫模態 (例如：Victoria mode，簡稱 VM) 有利於發展聖嬰/反聖嬰事件 (El Niño Southern Oscillation，簡稱 ENSO)。此研究利用觀測資料與數值模擬來探討結合北太平洋海溫變異與熱帶次表層熱含量對 ENSO 演變的影響。首先透過經驗正交函數的分析來檢驗次表層熱含量的氣候變異，其中第一與第二個模態為 ENSO 模態與它的相位轉換過程 (WWV)。交互相關分析指出這兩者氣候模態之間有著中度相關且約七個月的相位轉換，並且 WWV 的形成是透過中部赤道太平洋地區附近的風應力旋度所引起的經向副熱帶海洋環流(Subtropical cells)的變異，進而將水體注入至赤道地區逐漸形成 WWV。透過區分南北側近赤道區域的風應力旋度所造成經向水體運輸的分析，指出南北側的信風(Trade winds)距平將會對赤道地區注入熱含量，讓 WWV 更有利於發展 ENSO。這樣的結果能夠確認在 ENSO 的週期下改變熱帶地區熱含量的變異，不僅是由近赤道地區的海洋與大氣耦合動力下的貢獻，還有來自副熱帶地區信風變異的影響。

VM 是北太平洋中緯度海溫第二個氣候模態，並且有著典型的海溫足跡來影響熱帶地區的氣候動力。合成分析指出結合正(負)相位的 VM 與正(負)相位的 WWV 事件將有利於聖嬰(反聖嬰)事件的形成。主要的動力機制是 VM 的海溫變異能改變赤道地區的大氣環流且造成西風距平的生成，這樣的風場變異將能產生海洋凱爾文波(Kelvin waves)，並且將原先赤道地區的 WWV 向東傳遞來觸發 ENSO 事件。

本研究最後透過地球系統模式來驗證 VM 的貢獻對於 WWV 的改變所引起 ENSO 的發展。當 VM 與 WWV 指標皆是同個相位時，模式的表現將傾向於隨後幾個月發生 ENSO 事件。敏感度測試實驗指出如果持續地添加 VM 海溫變異至模式中，VM 與 Niño3.4 指標之間的關聯性將會提高，指出 ENSO 事件的發生裡 VM 是其中可控制的氣候因素。這樣的結果能夠確認 VM 與 WWV 是不同的氣候變異，

doi:10.6342/NTU202000712

並且皆是 ENSO 重要的預測指標。儘管最近的研究指出 WWV 在 2000 年以後不再是一個良好預測 ENSO 的指標，但是 2015-16 年的聖嬰事件能夠驗證結合 VM 與 WWV 的氣候變異能發展 ENSO 事件，並且如果考慮 VM 的變異能夠讓 WWV 更具有 ENSO 的可預報性。

關鍵字：聖嬰/反聖嬰現象、北太平洋海溫模態、暖水體、海洋熱含量、風應力旋度

doi:10.6342/NTU202000712

ABSTRACT

Previous studies suggested that both tropical subsurface heat content (i.e., Warm Water Volume, WWV) and the North Pacific sea surface temperature pattern (specifically Victoria Mode, VM), linked to the North Pacific sea level pressures, may tend to develop El Niño Southern Oscillation (ENSO) events. Here, we study the linkages between the VM and tropical ocean heat content within the ENSO evolution using the observation and model experiments. The first two dominant Empirical Orthogonal Function (EOF) modes of tropical ocean heat content represent the typical ENSO variation and its phase transition. Cross-correlation analysis indicates a moderate correlation of a 7-month phase lag between these two modes. The formation of WWV is directly caused by the meridional transport of Subtropical Cell driven by the wind stress curl. Separation of Sverdrup transport induced by the off-equatorial wind stress curl between northern and southern regions suggests that anomalous trade winds from both hemispheres may provide an additional charging of the subsurface heat content, leading to the WWV be conducive to develop the ENSO. These results confirm that not only coupled air-sea interactions near the tropics but also anomalous trade winds from the subtropics can modulate tropical subsurface heat content during the ENSO cycle.

The VM is defined as the second mode of sea surface temperature in the North Pacific, typical footprinting of the extratropical forcing on the tropical dynamics. Composite analysis confirms that the joint impacts of positive (negative) VM and positive (negative) WWV favor the development of El Niño (La Niña) events. The VM may favor the occurrence of anomalous westerlies in the tropics that drives oceanic Kelvin waves, causing the eastward propagation of WWV to trigger the ENSO events. The main contribution of VM on the WWV change leading to the ENSO development is verified using the Community Earth System Model. When the VM and WWV indices have the

doi:10.6342/NTU202000712

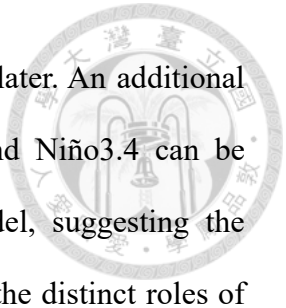

same sign, the model tends to develop ENSO events a few months later. An additional sensitivity experiment shows that the correlation between VM and Niño3.4 can be increased if the VM pattern is consistently imposed on the model, suggesting the controlling role of VM on the ENSO events. These results confirm the distinct roles of VM and WWV as the critical predictors of ENSO variability. Finally, although recent studies indicate that WWV is not a good predictor of ENSO events after 2000, the El Niño event in 2015-16 can verify that the joint impacts of VM and WWV variability on ENSO evolution, making the WWV more predictable about the ENSO event in consideration of the VM variability.

Keywords: El Niño Southern Oscillation, Victoria mode, warm water volume, ocean heat content, wind stress curl

doi:10.6342/NTU202000712

CONTENTS

doi:10.6342/NTU202000712

doi:10.6342/NTU202000712

LIST OF FIGURE

doi:10.6342/NTU202000712

doi:10.6342/NTU202000712

doi:10.6342/NTU202000712

doi:10.6342/NTU202000712

LIST OF FIGURE

doi:10.6342/NTU202000712

Chapter 1 Introduction

El Niño Southern Oscillation (ENSO) is the dominant climate variability that includes coupled air-sea interaction in the equatorial Pacific on interannual time scales. The sea surface temperature (SST) anomalies (SSTa) and their gradients in the tropics can lead to the anomalous wind stress which may modulate the subsurface heat content anomalies related to the ENSO cycle (Jin, 1997a; Jin, 1997b; Clarke et al., 2007). Considering the precursors of ENSO events, recent studies have explored the variations of subsurface heat content in the equatorial Pacific related to the ENSO cycle on the interannual time scales (Meinen & McPhaden, 2000; Meinen & McPhaden, 2001; Hasegawa & Hanawa, 2003). Meinen and McPhaden (2000) used isotherm 20℃ depth (D20) to determine subsurface heat content variability near the equator, and investigate the EOF modes of D20 anomalies (D20a) to explore the relationship between different D20a modes related ENSO cycle. The leading modes of D20a in the tropics show in Figure 1 (left panel). The D20a first mode is ENSO variability which is characteristic by zonal dipole oscillation pattern, while the D20a second mode is the warm water recharge-discharge mode which is characteristic by positive D20a over the equatorial Pacific basin. Furthermore, the D20a second mode serves as the warm water volume (WWV) variability (Bunge & Clarke, 2014), which is determined by the spatial integration of D20 near the whole equator region following by (Meinen & McPhaden, 2000). According to the analysis of Meinen and McPhaden (2000), the second mode leads the first mode by 7 months and it suggests that WWV may serve as a precursor of ENSO events. For more details about physical processes associated with subsurface heat content, Jin (1997a) has developed a framework of recharge oscillator that demonstrates how the zonal wind stress induced by zonal SST gradient near the equator can influence on zonal thermocline depth

doi:10.6342/NTU202000712

anomalies, and modify meridional Sverdrup transport to cause equatorial subsurface heat content variations. Also, wind stress curl variations near the equator may cause recharge or discharge of the warm water and its mechanism also relates to the ENSO dynamics (Clarke et al., 2007). However, although the WWV is useful to predict ENSO events, it is no longer a good predictor after 1998 because of the westward displacement of zonal wind stress forcing which may favorably contribute to the ENSO variability instead of the WWV variability (Bunge & Clarke, 2014). And the lead time of WWV variability may shorten because of the westward shift of the air-sea coupling near the equator, so it may lead to an increase of the ENSO frequency after 2000 (Hu et al., 2017). Although the WWV is not able to predict ENSO events at all, it is noted that the extratropical climate variability may be conducive to the development of ENSO events a year later and serve as another precursor of ENSO events in recent years (Ding et al., 2014; Ding et al., 2015).

Considering the impact of extratropical forcing on ENSO events, recently studies have investigated large-scale climate variability of air-sea physical processes from extratropical North Pacific which may trigger the onsets of the ENSO events (Vimont et al., 2001; Anderson, 2003; Vimont et al., 2003; Anderson, 2004), and have used coupled atmosphere-ocean model to investigate the impact of extratropical atmospheric variability on tropical climate (Vimont et al., 2009; Alexander et al., 2010). For example, the Victoria mode (VM), the second dominant Empirical Orthogonal Function (EOF) mode poleward of 20°N of monthly SSTa in the North Pacific may link the development of the ENSO (Ding et al., 2015). The EOF spatial distribution, corresponding Principal Component (VMI) and the seasonality of the VM are shown in Figure 2. The VM is caused by North Pacific Oscillation (NPO) which is represented as the second dominant mode of sea level pressure anomalies (SLPa) in the wintertime (Rogers, 1981; Linkin & Nigam, 2008) (Figure 2a). Furthermore, The VM is the basin-wide surface air-sea thermodynamic process with seasonal variability maximized during the springtime (February-March-

doi:10.6342/NTU202000712

April, FMA; Figure 2c), and it may interact with the subsurface ocean dynamic over the tropical Pacific to trigger ENSO events (Ding et al., 2015; Tseng et al., 2017).

The impacts of VM on triggering of ENSO involve the physical process of "seasonal footprinting mechanism" (Vimont et al., 2003); the subtropical SST footprints may be excited by extratropical sea level pressure anomalies associated with the NPO southern pole near the subtropics during the preceding winter. And when the NPO southern pole is an anomalous cyclone, it may weaken subtropical trade winds, decrease upward latent heat flux and subsequently generate positive SSTa. Thus, this positive air-sea feedback occurs and makes positive SSTa extend from subtropics to tropics during spring and summer (Vimont et al., 2001; Vimont et al., 2003). These SSTa variations near the equator may further modify the structure of atmospheric circulation by weakening equatorial trade winds, so the positive SSTa may occur to weaken zonal SST gradient and also cause strong anomalous westerlies near the equator. This positive ocean-atmosphere feedback is known as Bjerknes feedback and it is the coupled tropical ocean-atmosphere system that may trigger the onset of ENSO events (Bjerknes, 1969). However, it is noted that every strong VM is not always followed by the ENSO event and whether the VM triggers the ENSO event or not depends on the subsurface heat content variability near the tropics.

To combine the impact of extratropical and subtropical forcing with tropical subsurface heat content variability to discuss ENSO evolution, Anderson (2007) proposed that the subsurface heat content anomalies in the western Pacific previous autumn with the negative subtropical SLPa over the north Pacific in boreal winter tend to cause El Niño events 12~18 months later. It is also presumed that subtropical SLPa associated with the NPO may modify the subtropical winds stress to cause the meridional mass transport and induce recharge of equatorial heat content into the equator (Anderson & Perez, 2015).

doi:10.6342/NTU202000712

Finally, these processes give rise to accumulate subsurface heat content anomalies which may serve as a precursor of El Niño events. (Anderson et al., 2013; Anderson & Perez, 2015). On the other hand, the formation of WWV and its related physical processes before the development of ENSO events has been established by Chen et al. (2015), suggesting that the interior subtropical cells transport are related to the recharge or discharge of warm water on interannual time scales. However, the climate variability that may induce recharge or discharge of warm water before the formation of WWV has not been comprehensively understood. Also, most studies of extratropical air-sea processes have not comprehensively dealt with the relationship between extratropical forcing and tropical subsurface heat content variability.

Although many studies have brought out the importance of subsurface ocean conditions that initiate the onset of ENSO, no study exists yet in order to comprehensively discuss the relationship of the air-sea thermodynamic process about the VM and tropical ocean heat content variability with subsurface ocean dynamics. Therefore, our research objective is to investigate the linkages between the VM and tropical ocean heat content on ENSO evolution. How does the air-sea physical process linked with the VM influence the tropical subsurface heat content before ENSO events? What is the relationship between the VM and WWV? Does the VM lead to the formation of WWV? If not, what is the climate variability that may drive WWV variability? How does the evolution of ENSO variability when different conditions of the VM and WWV occur in the Pacific Ocean? Finally, this study used the Community Earth System Model (CESM) to explore the contribution of the VM forcing on ENSO development and ocean-atmosphere interactions in the Pacific Ocean.

doi:10.6342/NTU202000712

Chapter 2 Data and Method

2.1 Observation data

For this study, the subsurface ocean fields are taken from the European Centre of Medium-Range Weather Forecasts' oceanic reanalysis system product (ORA-S3) (Balmaseda et al., 2008). The monthly output data extends from 1959 to 2011 with a 1° spatial resolution off-equator and 0.3° near the equator, including wind stress, ocean salinity and ocean temperature about surface and subsurface. The SST from the Hadley Centre Global Sea Ice and Sea Surface Temperature (HadISST) which contains SST and sea ice variations for the period from 1871 to present (Rayner et al., 2006). For the atmospheric fields, we used sea level pressure (SLP), surface wind from National Centers for Environmental Prediction/National Center for Atmospheric Research (NCEP/NCAR) Reanalysis I for the period from 1959 to 2011 (Kalnay et al., 1996). All the anomalous fields are calculated by removing the annual cycle and linear trend before the statistical analysis.

2.2 Analysis methods

The empirical orthogonal function (EOF) and its associated principal components (PCs) are used here. Linear regression is also applied to identify the corresponding anomalous fields. Statistical significance is evaluated using the two-tailed student's t-test with an effective degree of freedom N^* defined by Bretherton et al. (1999) as follows:

$$N^* = \mathrm{N}\frac{1 - r_1 r_2}{1 + r_1 r_2}$$

where N is the total sample size and r_1 and r_2 are the autocorrelation of each time series.

To represent ENSO variability, we compute the Niño 3.4 index which averages SSTa

doi:10.6342/NTU202000712

over the tropical region (170°W~120°W, 5°S~5°N). Besides, we integrate the D20 to obtain the warm water volume (WWV) index over the tropical Pacific (120°E~80°W, 5°S~5°N) followed by Meinen and McPhaden (2000).

Based on the large-scale Sverdrup balance, we calculate the depth-integrated Sverdrup transport from the surface to the climatological 15℃ isotherm depth and examine the impact of meridional mass transport on the equatorial subsurface heat content following Anderson and Perez (2015). Sverdrup transport (V) is dominated by wind stress curl anomalies (first term of right-hand side) and vortex stretching of water mass (second term of right-hand side) (Clarke et al., 2007) shown as below:

$$V \approx \frac{\left(\frac{\partial \tau^y}{\partial x} - \frac{\partial \tau^x}{\partial y}\right)}{\beta \rho} + \frac{f}{\beta} \cdot \frac{\partial h_{15℃}}{\partial t} \quad (1)$$

where τ^x and τ^y are zonal and meridional wind stress, respectively. ρ is ocean density (here set the constant value of 1025 kg/m^3); f is Coriolis parameter; β is the beta parameter; and $\frac{\partial h_{15℃}}{\partial t}$ is the local main climatological thermocline depth with respect by time, as given by the depth of 15°C isotherm depth based on Deser et al. (2006). The Sverdrup transport should be balanced by large-scale wind stress curl anomalies and vortex stretching based on the monthly variability of the main thermocline depth.

2.3 Numerical models

The Community Earth System Model version 1.2.2 (CESM) used here is a fully-coupled global climate model that simulates the historical, present and future climate states (Hurrell et al., 2013). The CESM is composed of the atmospheric, ocean and other components. The atmospheric component is Community Atmospheric Model version 5.0 (CAM5) developed by NCAR with a horizontal resolution of 1.25°×0.9° and 30 vertical

doi:10.6342/NTU202000712

layers. The ocean component is the Parallel Ocean Program version 2 (POP2) from Los Alamos National Laboratory with the latitude and longitude resolution around 1° and 60 vertical layers. The control CESM initial condition is the same as CESM large ensembles in 1920, and we integrated for 80 years from 1921 to 2000 using 20-century historical forcing. An additional sensitive experiment is to examine the impact of VM forcing (VM SSTa pattern) on the ocean-atmosphere interactions over the Pacific and the ENSO evolution.

doi:10.6342/NTU202000712

Chapter 3 Result

3.1 Climate modes of tropical Pacific

To identify the climate modes of tropical D20a and SSTa associated with ENSO and WWV variability, we carry out an EOF analysis and cross-correlation analysis between their PCs. The first two dominant EOF modes of tropical D20a and SSTa are shown in Figure 1 while their corresponding PCs are normalized by themselves shown in Figure 3. The first EOF mode of D20a is characterized by a west-east dipole pattern with positive (negative) D20a near the eastern (western) equatorial Pacific (Figure 1a), and we refer to this mode as "tilt mode" in this study (Meinen & McPhaden, 2000). This is consistent with the first EOF mode of SSTa (i.e., the typical ENSO variability, represented by the Niño 3.4 index in Figure 3a), characterized by central and eastern warm SSTa patterns in the equatorial Pacific (Figure 1c). These results confirm that the first EOF mode of D20a, tilt mode, is also considered as the typical ENSO mode.

The second EOF mode of D20a is characterized by the positive D20a pattern located near the equatorial Pacific basin with a southern extension to the western South Pacific (Figure 1b). The consistency between the PC2 of D20a and the tropical WWV index in Figure 3b suggests that the PC2 of D20a shows the tropical WWV variability. We refer to this as "basin mode" in this study (Meinen & McPhaden, 2000). However, the second EOF mode of SSTa shows the typical El Niño Modoki with a positive (negative) SSTa pattern near the central (eastern) equatorial Pacific (Ashok et al., 2007) (Figure 1d) and this mode has been discussed extensively in the works of literature (Ashok et al., 2009; Kao & Yu, 2009; Kug et al., 2009; Yeh et al., 2009; Di Lorenzo et al., 2010; Yu & Kim, 2011; Kim et al., 2012).

We further verify the relationships between the PCs of SSTa and D20a using

doi:10.6342/NTU202000712

cross-correlation analysis (Figure 4). As expected, the PC1s of SSTa and D20a show a highly simultaneous correlation of 0.91 (Significant at 95% confidence level), suggesting the typical ENSO variability (Figure 4a). But the correlation between the first two PCs of SSTa (i.e., ENSO mode and El Niño Modoki), the correlation is generally low with the largest correlation of 0.22 occurs when the typical ENSO mode leads the El Niño Modoki by 6 months (Figure 4b) (but insignificant). This confirms that El Niño Modoki may be independent of typical ENSO variability (Ashok et al., 2007). Also, the insignificant cross-correlation (0.25 when El Niño Modoki leads the WWV by 8 months) between the PC2s of D20a and SSTa suggests that El Niño Modoki is independent of the WWV variability (Figure 4a).

However, the correlation between the PC1 and PC2 of D20a shows a positive correlation of 0.38 when the basin mode leads the tilt mode by 6 months, while it also shows the negative correlation of -0.65 (Significant at confidence level 95%) when the tilt mode leads to the basin mode by 7 months (Figure 4b). It can demonstrate that the positive WWV may occur before the typical El Niño, and also the El Niño may subsequently lead to the negative WWV. The relationship between the WWV and ENSO variability is agreed with previous studies, suggesting the recharge and discharge processes of warm water induced by anomalous wind stress curl near the tropics may modulate ENSO cycle and its phase transition (Jin, 1997a; Clarke et al., 2007; Chen et al., 2015).

3.2 Sverdrup transport related to tropical ocean heat content variability

Considering the possible mechanisms associated with the first two leading modes of tropical D20a, we regress the simultaneous Sverdrup transport and its related terms onto the first two PCs of D20a in Figure 5. For the tilt mode, the strengthened tropical westerly

doi:10.6342/NTU202000712

winds provide positive (negative) wind stress curls near the northern (southern) off-equatorial regions, leading to northward (southward) Sverdrup transport (Figure 5a). Therefore, the water mass may discharge poleward from the equator. The wind stress curl term (the 1st term in the right-hand side of Eqn. 1) dominants the Sverdrup transport as expected since its spatial pattern resembles the total Sverdrup transport between 10°S and 10°N with mass transport divergence (Figure 5b). Compared with the wind stress curl term, the vortex stretching term (the 2nd term in the Eqn. 1) shows a smaller contribution to the total Sverdrup transport. The dominant wind stress curl term induces the divergence of Sverdrup transport near the equatorial region (160°E~140°W, 5°S~5°N) during positive tilt mode (i.e., El Niño).

For the basin mode, the positive D20a is located over the equatorial Pacific basin with slight mass transport along the tropics (Figure 5d). Compared with the strong wind stress anomalies near the equatorial region (160°E~140°W, 5°S~5°N) in the tilt mode, weak wind stress anomalies in the basin mode contributes to the weak Sverdrup transport with a weak convergence near the tropic (Figure 5d). Again, the wind stress curl term associated with the basin mode also bears a resemblance to the sum of Sverdrup transport near the equator (Figure 5e) while the vortex stretching term has a weaker contribution (Figure 5f). Therefore, the basin mode may also link to the Sverdrup transport driven by wind stress curl anomalies. However, some issues remain to be discussed. What is the relationship between the Sverdrup transport convergence/divergence and the leading modes of tropical D20a in time? To further address this, we show the cross-correlation between the Sverdrup transport time series and the first two leading PCs of tropical D20a in Figure 6. The Sverdrup transport time series and its contributed terms are calculated by the net equatorward mass transport along 5°S and 5°N. Positive (negative) correlations represent the Sverdrup transport convergence (divergence). As expected, the tilt mode associated with strong westerly near the equator induces the divergence of Sverdrup

doi:10.6342/NTU202000712

transport (correlation is -0.60 between the wind stress curl term and the tilt mode, significant at 95% confidence level). In contrast, the vortex stretching term has no significant correlation with the tilt mode (Figure 6a). For the basin mode in Figure 6b, the Sverdrup transport leads the basin mode by 8 months with a correlation of 0.49 (Significant at 95% confidence level). This indicates that the convergence of Sverdrup transport may induce the warm water recharged into the equator a few months later, leading to the basin mode. Again, the wind stress curl plays a dominant role in the Sverdrup transport, contributing to the basin mode change, rather than the vortex stretching. Overall, these results can be view as the recharge process of interior subtropical cells driven by the wind stress curl, causing the subsurface heat content to accumulate near the equator and finally form the positive WWV by a quarter cycle phase (Chen et al., 2015). And the WWV initiates the positive SSTa that may induce anomalous westerlies, tilting the thermocline depth near the equator, so this positive air-sea feedback finally triggers the El Niño. Subsequently, the tilt mode with the discharge of subsurface heat content can also be viewed as the discharge process of interior subtropical cells and finally form the negative basin mode by a quarter of the ENSO cycle.

3.3 The wind stress curl related to tropical ocean heat content variability

Where can the wind stress curl have a critical impact on the Sverdrup transport thus changing the tropical D20a modes? Here, we examine the correlation map between the first two leading PCs of tropical D20a and the wind stress curl term.

For the tilt mode (Figure 7), before the mature state of the El Niño, positive correlations of D20a (contours) near the central-eastern equatorial Pacific are gradually established (Figure 7. lag -6 ~ lag 0). This suggests the WWV is formed and propagated eastward until the matured El Niño. When the tilt mode is the well-established, positive

doi:10.6342/NTU202000712

(negative) correlation of wind stress curl term occurs around 5°N (5°S) latitude (Figure 7. lag 0). This pattern induces the discharge of warm water and subsequently form the negative basin mode with negative correlations of D20a along the equatorial Pacific basin a few months later (Figure 7. lag +3 ~ +9, also Figure 4b), consistent with the previous study (Chen et al., 2015) that the divergent transport of subtropical cells can discharge warm water on interannual time scales.

For the basin mode (Figure 8), positive (negative) correlations of D20a near the western (eastern) Pacific occur at lag -9, accompanied by negative (positive) correlation of wind stress curl term along 5°N (5°S). This La Niña pattern may further recharge the WWV and subsequently form the positive basin mode along the equatorial Pacific (Figure 8. lag -6 ~ 0). Thus, this result indicates that the formation of WWV is caused by the meridional transport of subtropical cells driven by the wind stress curl during ENSO events.

3.4 The evolution of subsurface heat content

3.4.1 Tilt mode

To explore the evolution of the first two leading modes of tropical D20a, we show the composite analysis of D20a, Sverdrup transport anomalies, wind stress anomalies, and subsurface heat content onto the PC1 of the D20a (tilt mode) in Figures 9 and 10. We choose the typical El Niño events in 1965-66, 1972-73, 1982-83, 1986-87, 1991-92, 1994-95, 1997-98, 2002-03 and 2009-10.

15 months before the mature of tilt mode, the positive D20a is located near the western tropical Pacific (Figure 9. SON(-1)). Anderson (2007) found that the subsurface heat content anomaly near the western Pacific is a crucial precursor 12 ~ 15 months before the mature stage of ENSO events. Subsequently, anomalous trade winds around the

doi:10.6342/NTU202000712

the off-equatorial region between 180° to 140°W appear, and they are related to negative wind stress curls cause southward Sverdrup transport that may recharge subsurface heat content into the equator (Figure 9. DJF(0) ~ MAM(0)) (Anderson & Perez, 2015). Thus, this mechanism leads to the emergence of positive basin mode in the equatorial Pacific, and equatorial anomalous westerlies subsequently induce downwelling oceanic Kelvin waves, leading to the propagation of positive D20a along the equator (Figure 9. JJA(0) ~ SON(0)). This positive WWV may warm the SST near the eastern Pacific and cause anomalous deep convention, affecting the wind stress curl near off-equatorial regions (Gill, 1982). At the same time, accumulating negative D20a near the western tropical Pacific is associated with the westward propagation of upwelling Rossby waves induced by Ekman pumping driven by the off-equatorial wind stress curl (Figure 9. JJA(0) ~ SON(0)) (Kessler, 1990; White et al., 2003). Because of the continuously westward propagation of positive D20a and eastward propagation of negative D20a, the tilt mode (El Niño) is well established with positive (negative) D20a near the eastern (western) tropical Pacific (Figure 9. DJF(+1)). After the mature state of the El Niño, the strong anomalous westerlies induce the divergence of Sverdrup transport, so the warm water starts to discharge between 160°E and 140°W (Figure 9. MAM(+1) ~ JJA(+1)). Thus, negative D20a starts to emerge along with the equatorial band and finally forms the negative basin mode (Figure 9. SON(+1)).

The change of D20a and Sverdrup transport is directly linked to the subsurface heat content anomalies. Figure 10 shows the evolution of equatorial subsurface temperature (averaged between 2°S and 2°N) associated with the PC1 of the D20a (tilt mode). Warm water anomalies can be identified above 15℃ isotherm depth (Figure 10. SON(-1) ~ DJF(0)) in the western tropical Pacific. When the anomalous westerlies begin to trigger downwelling oceanic Kelvin waves, positive temperature anomalies gradually propagate eastward along the isotherms (Figure 10. DJF(0) ~ JJA(0)). As soon as the warm water

doi:10.6342/NTU202000712

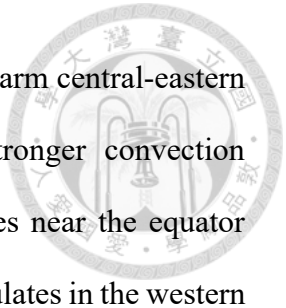

begins to upwell toward the surface near the eastern Pacific, it may warm central-eastern Pacific SST and feedback to atmospheric circulation through stronger convection (Bjerknes, 1969). This can further enhance the anomalous westerlies near the equator (Figure 10. JJA(0) ~ DJF(+1)). Also, the negative heat content accumulates in the western half basin because of upwelling Rossby waves caused by Ekman pumping driven by the off-equatorial wind stress curl (Figure 10. JJA(0) ~ DJF(+1)) (Kessler, 1990; White et al., 2003). Thus, typical El Niño occurs with positive (negative) subsurface heat content near the eastern (western) basin. Subsequently, the divergence of Sverdrup transport starts during the mature stage of the El Niño, the positive (negative) subsurface heat content anomalies around 160°E to 140°W are then reduced (enhanced) (Figure 10. DJF(+1) ~ JJA(+1)). Therefore, the cold anomalies gradually occur along with the isotherm to weaken the positive SSTa near the central-eastern Pacific, weakening the equatorial zonal SSTa gradient and anomalous westerlies (Figure 9. MAM(+1) ~ SON(+1)). Finally, the divergence of Sverdrup transport is terminated, forming the negative basin mode with negative subsurface heat content around the basin (Figure 10. SON(+1)).

3.4.2 Basin mode

Next, a similar surface and subsurface evolution of the basin mode will be discussed. We choose the typical La Niña events in 1971-72, 1975-76, 1996-97, 2007-08 and 2008-09, followed by the basin mode that may be conducive to the next El Niño event. Around 3 to 6 months before the basin mode in MAM(0) season, we can see the negative tilt mode (La Niña) with positive (negative) D20a near the western (eastern) Pacific (Figure 11. SON(-1) ~ DJF(0)). This typical La Niña is accompanied by strong anomalous easterlies, which may induce the convergence of Sverdrup transport around 160°E to

doi:10.6342/NTU202000712

140°W. The warm water gradually recharges into the central tropical Pacific (Figure 11. DJF(0)). Finally, the positive basin mode occurs with weak wind anomalies around the central equatorial Pacific (Figure 11. MAM(0)). The Sverdrup transport convergence is terminated. The warm water starts to propagate eastward in response to anomalous westerlies and subsequently form the positive tilt mode (El Niño) (Figure 11. JJA(0) ~ DJF(+1)).

Again, we also analysis the subsurface heat content anomalies about the basin mode. As expected, before the positive basin mode, negative tilt mode (La Niña) with negative (positive) temperature near the eastern (western) half basin is found (Figure 12. SON(-1) ~ DJF(0)). Subsequently, the positive temperature anomalies may extend eastward along with the isotherms by the recharge of warm water in response to anomalous easterlies with the La Niña. Afterward, the warm water begins upwelling toward the surface to modify the SST (Figure 12. JJA(0) ~ DJF(+1)) and leads to positive tilt mode (El Niño).

Finally, we examine the time evolution of Sverdrup transport driven by wind stress curl term and D20a variations separation between northern regions (2°N ~ 3°N, 5°N and 10°N) and southern regions (2°S ~ 3°S, 5°S and 10°S) onto the first and second modes of D20a shown in Figure 13 and 14, respectively. For the tilt mode (Figure 13), the formation of positive D20a might be accumulated by the southward Sverdrup transport (blue shading) from northern regions between 2°N and 5°N near the central Pacific around 9 to 18 months ago (Figure 13a, b). Also, northward Sverdrup transport (red shading) near southern regions between 2°S and 10°S in the eastern Pacific may enhance the positive D20a around 3 to 12 months ago (Figure 13 d-f). These results are associated with northern anomalous trade winds modulating subsurface heat content before the ENSO events (Figure 9. DJF(0) ~ MAM(0)) (Anderson et al., 2013), and is also linked with southern anomalous trade winds which might enhance heat content near the eastern

doi:10.6342/NTU202000712

Pacific (Figure 9. JJA(0) ~ SON(0)). After the tilt mode, northern regions show northward Sverdrup transport between 2°N and 5°N near the central Pacific while southern regions show southward Sverdrup transport between 5°S and 10°S.

For the basin mode (Figure 14), northern regions show significantly southward Sverdrup transport 2°N and 5°N near the central-eastern Pacific around 3 to 12 months ago (Figure 14a, b) while southern regions show significantly northward Sverdrup transport between 5°S and 10°S (Figure 14 e-f). Also, it is noted that eastward propagations of northward Sverdrup transport show in southern regions due to the zonal shift of air-sea coupled regions (Figure 14 d-f), consistent with the wind stress curl shown in Figure 8 and the D20a spatial distribution shown in Figure 11 (SON(-1) ~ JJA(0)). These results indicate that the wind stress curl from both northern and southern off-equatorial regions has an important impact on the recharge or discharge of equatorial subsurface heat content. Thus, there are some issues need to be addressed. Can the wind stress curl near the tropics induced by the VM cause the modulation of subsurface heat content and even WWV variability to trigger ENSO events? How does the evolution of ENSO variability when different conditions of VM and WWV in the Pacific ocean?

doi:10.6342/NTU202000712

Chapter 4 The link between the VM and tropical WWV

4.1 The relationship between the VM and tropical climate variability

In section 3, we have confirmed the relationship of tropical D20a with SSTa and understood the physical processes about the first two leading modes of tropical D20a. Now, we further explore the relationship between the VM and tropical variability of SSTa and D20a using the cross-correlation analysis (Figure 15). The VMI leads the PC1 of SSTa and D20a by 6 and 11 months with a correlation coefficient of 0.31 and 0.32 (Significant at 95% confidence level), respectively. However, it has no significant correlation with the PC2 of SSTa and D20a, so the VM may be independent of El Niño Modoki and the basin mode. Because of the low correlation between the VM and the basin mode, we define the year of positive (negative) VM event and positive (negative) WWV event by their indices greater (lower) than 0.7 standard deviations in February-March-April (FMA) season (Figure 16). Different conditions of the VM and WWV events are used to investigate the joint impacts of VM and WWV on the subsequent development of ENSO events or not (Table 1). It is likely the joint of positive (negative) VM and positive (negative) WWV may develop El Niño (La Niña) events. On the other hand, the joint of positive (negative) VM and negative (positive) WWV may not necessarily be followed by El Niño (La Niña) events. We will further explore the physical processes associated with this joint impact next.

4.2 The composite analysis of different states of VM and WWV events

We first examine the composite of positive VM and positive WWV followed by El

doi:10.6342/NTU202000712

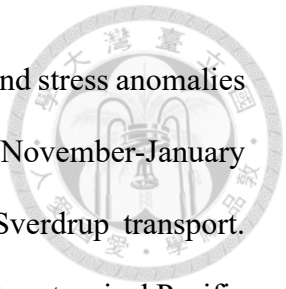

Niño events. Figure 17 shows the composite of SSTa and D20a and wind stress anomalies for the period from August-October ASO(-1) one year in advance to November-January NDJ(+1). The composite of wind stress curl term contributed to Sverdrup transport. During ASO(-1), the positive D20a has already appeared near the western tropical Pacific (might be weak La Niña-negative tilt mode in 1964-65). During NDJ(0) to FMA(0), the positive WWV is well established with anomalies southwesterlies and weak equatorward Sverdrup transport (Figure 18). When VM pattern extends into the tropics in FMA(0) with anomalous southwesterlies, the positive WWV begins to propagate eastward and modulate the zonal SSTa gradient to strength anomalous westerlies near the equator during FMA(0) to ASO(0), leading to the El Niño (tilt mode) and strong anomalous westerlies which can further enhance the Sverdrup transport divergence in the tropic.

Similarly, Figures 19 and 20 show the same composites of SSTa and the Sverdrup transport contributed by wind stress curl term for the negative VM and WWV. The physical processes are completely opposite as expected.

doi:10.6342/NTU202000712

Chapter 5 The result of numerical models

5.1 Climate modes of tropical Pacific variability

We now turn to analyze the tropical SSTa and D20a in the CESM control run (CTRL) to examine the hypothesis we proposed. The spatial patterns of tropical SSTa and D20a in the coupled model are shown in Figure 21. Similar to the reanalysis products, the first EOF mode of D20a shows zonal dipole pattern with positive (negative) D20a near the eastern (western) Pacific (Figure 21a) while the first EOF mode of SSTa shows the warm SST pattern in the central-eastern Pacific (Figure 21c). These first modes have a highly simultaneous correlation of 0.96 (Significant at 95% confidence level) (Figure 22a). The second EOF mode of D20a shows positive D20a over equatorial basin Pacific (Figure 21b). For the cross-correlation between the PC1 and PC2 for the D20a, it shows the positive correlation above 0.48 (Significant at 95% confidence level) when the basin mode leads the tilt mode by 12 to 15 months and negative correlation of -0.72 (Significant at 95% confidence level) when the tilt mode leads to the basin mode by 9 months (Figure 22b). The SSTa second EOF shows a positive horseshoe-like SST pattern extended into the subtropics and a cool SST pattern near the eastern equatorial Pacific, and it might be generated by the subtropical air-sea feedback that has an impact on the tropical climate system. Because it has low correlations with the PC1 of SSTa and the PC2 of D20a (Figure 22), this mode might be independent of typical ENSO and WWV variability in CESM.

5.2 The Victoria mode and its relationship with tropical climate modes

doi:10.6342/NTU202000712

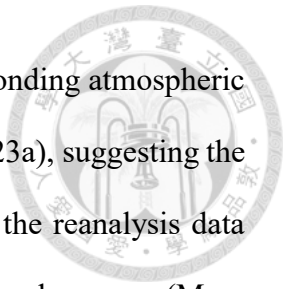

We further investigated the modeled VM pattern and its corresponding atmospheric fields in Figure 23a. A clear NPO-like wind pattern is shown (Figure 23a), suggesting the direct impact of NPO on the VM in the CTRL run, consistent with the reanalysis data (Figure 2a). But the seasonality of the VM reaches its peak around boreal summer (May-June-July) (Figure 23b). For the cross-correlation between the VM and tropical climate modes in Figure 24, the VM index leads the PC1 of tropical D20a and SSTa by around 9 to 10 months (correlations of 0.34 and 0.36; significant at 95% confidence level). These results indicate that the VM might be independent of the basin mode and El Niño Modoki-like pattern in CTRL run and it might lead ENSO variability by a few months, consistent with the results from ECMWF reanalysis.

5.3 Model experiment design

We perform an additional sensitivity experiment to examine the impact of VM on the simulation. Using the HadiSST data, we regress the North Pacific SSTa onto the VM index in the FMA season to represent this VM pattern (Figure 25). We add this VM-forcing to the modeled FMA SST in the CESM simulation every year and integrate the simulation (VMP run) for 80 years (1921 to 2000). The last 70 years are used to explore climate variability. Our purpose is to examine the contribution of VM forcing on ENSO evolution and also explore the ocean-atmosphere interactions over the Pacific Ocean. Figure 23b shows the VM and its corresponding atmospheric fields in the VMP run. The pattern is similar to that of the CTRL run (Figure 23a). It is interesting to see that the seasonality of the VM reaches the peak around the FMA season (Figure 23d), consistent with the observation. Its standard deviation increases slightly compared to the result of the CTRL run.

doi:10.6342/NTU202000712

5.4 The relative contribution of VM and WWV variability on ENSO

We further explore the differences between these two runs. First, the relative contribution of VM and WWV on ENSO is examined using the cross-correlation of the Niño 3.4 index with VM and WWV indices (Figure 26). In the CTRL run, the VM index leads the Niño 3.4 index by 9 months with a correlation of 0.36 (Significant at 95% confidence level). WWV leads Niño 3.4 index by 13 months with a correlation of 0.44, and it also lags the Niño 3.4 index by 7 months with a correlation of -0.75 (Significant at 95% confidence level). As to the VMP run, the lead-lag time between WWV and Niño 3.4 index is consistent with the result of the CTRL run. However, the VM index leads Niño 3.4 index by 12 months with the correlation of 0.37 (Significant at 95% confidence level), so when we imposed the positive VM pattern into the model, it appears a 3-month time shift of lead-lag time between VM and Niño 3.4 index in the VMP run.

Second, we focus on the correlation of the DJF(+1) Niño 3.4 index with different seasons of VM and WWV indices. For the seasonal correlation between WWV and Niño 3.4 index, both runs show the highest correlation between the DJF(0) WWV and DJF(+1) Niño 3.4 index (Figure 27a, c). But for the seasonal correlation between VM and Niño 3.4 indices, the AMJ(0) VM index correlates well with DJF(+1) Niño 3.4 index in the CTRL run while the JFM(0) VM index correlates best in the VMP run (Figure 27b, d). As indicated previously, these results confirm that imposing the positive FMA VM pattern into the CESM simulation may shift the VM and Niño 3.4 index relation 3 months earlier in VMP run.

Finally, the relative contribution of the VM and WWV variability on ENSO is examined. We compute the correlations of DJF(0)-averaged WWV and AMJ(0)-averaged VM indices with the following boreal winter DJF(+1)-averaged Niño 3.4 index for the CTRL run (Figure 28). If both VM and WWV indices have the same sign, the correlation

doi:10.6342/NTU202000712

between the WWV and Niño 3.4 indices is 0.74 (Significant at 95% confidence level; Figure 28b), which is much higher than the correlation between VM and Niño 3.4 indices (R = 0.59; Significant at 95% confidence level; Figure 28a). In contrast, if the VM and WWV indices have opposite signs, the correlations of the VM and WWV indices with the Niño 3.4 index are very low (R = 0.20 and R = -0.12; Not significant at 95% confidence level; Figure 28c and 28d, respectively). These suggest that the WWV variability is relatively more prominent for developing the ENSO event. Also, combining both WWV and VM together can greatly lead to ENSO events.

Similarly, we also calculate the correlations of DJF(0)-averaged WWV and JFM(0)-averaged VM indices with the following boreal winter DJF(+1)-averaged Niño 3.4 index for the VMP run (Figure 29). If both the VM and WWV indices have the same sign, the correlation between the WWV and Niño 3.4 indices is 0.72 (Significant at 95% confidence level; Figure 29b), which is also higher than the correlation between the VM and Niño 3.4 indices (R = 0.65; Significant at 95% confidence level; Figure 29a). For the opposite sign of the VM and WWV indices, the correlations of VM and WWV indices with Niño 3.4 index are low (R = 0.07 and R = 0.30; Not significant at 95% confidence level; Figure 29c and 29d, respectively). Therefore, when the VM and WWV indices have the same sign, the model tends to develop ENSO events a few months later. The VMP run shows that the correlation between the VM and Niño3.4 indices can be increased if the VM pattern is consistently imposed on the model in FMA season, suggesting that including the VM can increase additional predictability on the development of the ENSO system in the model simulation (Chen et al., 2020).

5.5 The composite analysis of VM and WWV variability

Finally, we examine the evolution in the years when both the VM and WWV indices

doi:10.6342/NTU202000712

have the same sign. Figure 30 shows the composite of the positive sign of the VM and WWV indices in the CTRL run. The positive WWV has already appeared in the western-central equatorial Pacific in the previous year (Figure 30. ASO(-1) ~ NDJ(0)). When the positive VM extends into the tropics through the coupled air-sea thermodynamics (Figure 30. FMA(0)), the anomalous westerlies make positive WWV propagate eastward and subsequently warm the SSTa in the eastern tropical Pacific (Figure 30. MJJ(0) ~ ASO(0)). Finally, this positive air-sea feedback in the tropics develops El Niño events with a typical tilt mode pattern. Thus, these results confirm that the joint of positive VM and positive WWV may develop a typical El Niño event in CTRL run, consistent with the results from ECMWF reanalysis. And the warm water of positive tilt mode requires positive WWV over equatorial Pacific about 12 months ago. A similar evolution pattern can be found in the composite of the negative sign of the VM and WWV indices in the CTRL run (Figure 31). The joint of negative VM and negative WWV can lead to the typical La Niña events in the CTRL run. Also, the cool water of negative WWV should have negative basin mode before.

Similar evolution for both composite years can be found in the VMP run (both positive sign in Figure 32 and both negative sign in Figure 33) except the timing is changed slightly. In summary, the model simulation for both runs confirms the typical ENSO requires a positive VM pattern to enhance the WES feedback associated with the trade winds anomalies near the subtropics. Combining the VM and WWV variability may effectively develop the ENSO events.

doi:10.6342/NTU202000712

Chapter 6 Conclusion

This study confirms the first two leading EOF modes of 20℃ isotherm depth as subsurface heat content variations. The first mode is the tilt mode that is the typical ENSO variability, while the second mode is the basin mode (WWV variability). The cross-correlation analysis shows that these two modes have a 7-months lead-lag time phase shift. Positive basin mode leads to positive tilt mode (El Niño), and positive tilt mode leads to negative basin mode. The wind stress curl term contributing to the Sverdrup transport plays a critical role in the change of tropical D20a and is associated with subtropical cells that may regulate the ENSO cycle. Separation of Sverdrup transport induced by the off-equatorial wind stress curl between northern and southern regions suggests that anomalous trade winds from both hemispheres may provide an additional charging of the subsurface heat content, leading to the WWV favor to develop the ENSO event. These results confirm that not only coupled air-sea interactions near the tropics but also anomalous trade winds from the subtropics can modulate tropical subsurface heat content during the ENSO cycle.

Composite analysis confirms that the joint impacts of positive (negative) VM and (negative) WWV variability may be conducive to the development of El Niño (La Niña) events. Because the VM with air-sea thermodynamics may lead to the occurrence of anomalous westerlies in the tropics, it may further drive oceanic Kelvin waves in the tropic, causing the WWV to propagate eastward and trigger the ENSO events. Also, this study uses the Community Earth System Model to verify the main contribution of VM on ENSO development. Results show that the VM and WWV indices have the same sign, the model facilitates the development of ENSO events a few months later. An additional sensitivity experiment shows that the correlation between VM and Niño3.4 indices can

doi:10.6342/NTU202000712

be increased if the VM pattern is consistently imposed on the model, suggesting the controlling role of VM on the ENSO events.

Although the WWV is not a good predictor of ENSO events in recent years, it can still verify the joint impacts of VM and WWV variability on the 2015-16 El Niño event (Figure 34). Before the El Niño events about 12 to 15 months, WWV has already been located near the tropics (Figure 34. SON(-1) ~ DJF(0)). Because of the VM forcing with enhancing positive D20a driven by anomalous trade winds in FMA(0) season, WWV is conducive to develop El Niño event a few months later. Thus, the WWV linked with the VM variability can be more predictable about the ENSO event.

Previous studies have indicated that both SST footprints from North Pacific extratropical regions and tropical WWV are linked to the onset of ENSO development. Our study supports the insights for the ENSO evolution that both the equatorial wind anomalies triggered by the VM forcing and the WWV variability due to the meridional transport of subtropical cells can contribute to the ENSO events. An issue that was not addressed in this study whether every typical ENSO followed by equatorial wind anomalies triggered by the VM forcing. Here, we only focus on the North Pacific extratropical impacts of VM on tropical ocean heat content since this impact becomes more prominent after 2000. The impact of South Pacific extratropical forcing should also be considered. Recent studies have found that South Pacific extratropical atmospheric variability via the seasonal footprinting mechanism may have an additional influence on ENSO (Ding et al., 2014; You & Furtado, 2017). By considering both North and South Pacific SST anomalies with coupled air-sea thermodynamics may improve the prediction of ENSO events (Ding et al., 2019). Further studies need to explore how the combination of North and South Pacific climate variability influences tropical subsurface heat content.

doi:10.6342/NTU202000712

REFERENCE

Alexander, M. A., Vimont, D. J., Chang, P., & Scott, J. D. (2010). The Impact of Extratropical Atmospheric Variability on ENSO: Testing the Seasonal Footprinting Mechanism Using Coupled Model Experiments. *Journal of Climate, 23*(11), 2885-2901. doi:10.1175/2010jcli3205.1

Anderson, B. T. (2003). Tropical Pacific sea-surface temperatures and preceding sea level pressure anomalies in the subtropical North Pacific. *Journal of Geophysical Research, 108*(D23). doi:10.1029/2003jd003805

Anderson, B. T. (2004). Investigation of a large-scale mode of ocean–atmosphere variability and its relation to tropical Pacific sea surface temperature anomalies. *17*(20), 4089-4098.

Anderson, B. T. (2007). On the Joint Role of Subtropical Atmospheric Variability and Equatorial Subsurface Heat Content Anomalies in Initiating the Onset of ENSO Events. *Journal of Climate, 20*(8), 1593-1599. doi:10.1175/jcli4075.1

Anderson, B. T., & Perez, R. C. (2015). ENSO and non-ENSO induced charging and discharging of the equatorial Pacific. *Climate Dynamics, 45*(9-10), 2309-2327. doi:10.1007/s00382-015-2472-x

Anderson, B. T., Perez, R. C., & Karspeck, A. (2013). Triggering of El Niño onset through trade wind-induced charging of the equatorial Pacific. *Geophysical Research Letters, 40*(6), 1212-1216. doi:10.1002/grl.50200

Ashok, K., Behera, S. K., Rao, S. A., Weng, H., & Yamagata, T. (2007). El Niño Modoki and its possible teleconnection. *Journal of Geophysical Research, 112*(C11). doi:10.1029/2006jc003798

Ashok, K., Tam, C. Y., & Lee, W. J. (2009). ENSO Modoki impact on the Southern Hemisphere storm track activity during extended austral winter. *Geophysical Research Letters, 36*(12). doi:10.1029/2009gl038847

Balmaseda, M. A., Vidard, A., & Anderson, D. L. T. (2008). The ECMWF Ocean Analysis System: ORA-S3. *Monthly Weather Review, 136*(8), 3018-3034. doi:10.1175/2008mwr2433.1

Bjerknes, J. (1969). Atmospheric teleconnections from the equatorial Pacific. *MONTHLY WEATHER REYIEW*. doi:UDC 551.513:551.508.338:551.465.6(265)(267)

Bretherton, C. S., Widmann, M., Dymnikov, V. P., Wallace, J. M., & Bladé, I. (1999). The effective number of spatial degrees of freedom of a time-varying field. *Journal of Climate, 12*(7), 1990-2009.

Bunge, L., & Clarke, A. J. (2014). On the Warm Water Volume and Its Changing Relationship with ENSO. *Journal of Physical Oceanography, 44*(5), 1372-1385. doi:10.1175/jpo-d-13-062.1

doi:10.6342/NTU202000712

Chen, H.-C., Sui, C.-H., Tseng, Y.-H., & Huang, B. J. J. o. C. (2015). An analysis of the linkage of Pacific subtropical cells with the recharge–discharge processes in ENSO evolution. *28*(9), 3786-3805.

Chen, H. C., Tseng, Y. H., Hu, Z. Z., & Ding, R. (2020). Enhancing the ENSO Predictability beyond the Spring Barrier. *Sci Rep, 10*(1), 984. doi:10.1038/s41598-020-57853-7

Clarke, A. J., Van Gorder, S., & Colantuono, G. (2007). Wind Stress Curl and ENSO Discharge/Recharge in the Equatorial Pacific. *Journal of Physical Oceanography, 37*(4), 1077-1091. doi:10.1175/jpo3035.1

Deser, C., Capotondi, A., Saravanan, R., & Phillips, A. S. (2006). Tropical Pacific and Atlantic climate variability in CCSM3. *Journal of Climate, 19*(11), 2451-2481.

Di Lorenzo, E., Cobb, K. M., Furtado, J. C., Schneider, N., Anderson, B. T., Bracco, A., . . . Vimont, D. J. (2010). Central Pacific El Niño and decadal climate change in the North Pacific Ocean. *Nature Geoscience, 3*(11), 762-765. doi:10.1038/ngeo984

Ding, R., Li, J., & Tseng, Y.-h. (2014). The impact of South Pacific extratropical forcing on ENSO and comparisons with the North Pacific. *Climate Dynamics, 44*(7-8), 2017-2034. doi:10.1007/s00382-014-2303-5

Ding, R., Li, J., Tseng, Y.-h., Sun, C., & Guo, Y. (2015). The Victoria mode in the North Pacific linking extratropical sea level pressure variations to ENSO. *Journal of Geophysical Research: Atmospheres, 120*(1), 27-45. doi:10.1002/2014jd022221

Ding, R., Tseng, Y. h., Li, J., Sun, C., Xie, F., & Hou, Z. (2019). Relative contributions of North and South Pacific sea surface temperature anomalies to ENSO. *Journal of Geophysical Research: Atmospheres*. doi:10.1029/2018jd030181

Gill, A. (1982). Atmosphere–Ocean Dynamics. Academic Press, 662 pp.

Hasegawa, T., & Hanawa, K. J. J. o. p. o. (2003). Heat content variability related to ENSO events in the Pacific. *33*(2), 407-421.

Hu, Z. Z., Kumar, A., Zhu, J., Huang, B., Tseng, Y. H., & Wang, X. (2017). On the Shortening of the Lead Time of Ocean Warm Water Volume to ENSO SST Since 2000. *Sci Rep, 7*(1), 4294. doi:10.1038/s41598-017-04566-z

Hurrell, J. W., Holland, M. M., Gent, P. R., Ghan, S., Kay, J. E., Kushner, P. J., . . . Marshall, S. (2013). The Community Earth System Model: A Framework for Collaborative Research. *Bulletin of the American meteorological Society, 94*(9), 1339-1360. doi:10.1175/bams-d-12-00121.1

Jin, F.-F. (1997a). An equatorial ocean recharge paradigm for ENSO. Part I: Conceptual model. *Journal of the Atmospheric Sciences, 54*(7), 811-829.

Jin, F.-F. (1997b). An equatorial ocean recharge paradigm for ENSO. Part II: A stripped-down coupled model. *Journal of the Atmospheric Sciences, 54*(7), 830-847.

Kalnay, E., Kanamitsu, M., Kistler, R., Collins, W., Deaven, D., Gandin, L., . . . Woollen,

doi:10.6342/NTU202000712

J. (1996). The NCEP/NCAR 40-year reanalysis project. *Bulletin of the American meteorological Society, 77*(3), 437-472.

Kao, H.-Y., & Yu, J.-Y. (2009). Contrasting Eastern-Pacific and Central-Pacific Types of ENSO. *Journal of Climate, 22*(3), 615-632. doi:10.1175/2008jcli2309.1

Kessler, W. S. (1990). Observations of long Rossby waves in the northern tropical Pacific. *Journal of Geophysical Research, 95*(C4). doi:10.1029/JC095iC04p05183

Kim, S. T., Yu, J.-Y., Kumar, A., & Wang, H. (2012). Examination of the Two Types of ENSO in the NCEP CFS Model and Its Extratropical Associations. *Monthly Weather Review, 140*(6), 1908-1923. doi:10.1175/mwr-d-11-00300.1

Kug, J.-S., Jin, F.-F., & An, S.-I. (2009). Two Types of El Niño Events: Cold Tongue El Niño and Warm Pool El Niño. *Journal of Climate, 22*(6), 1499-1515. doi:10.1175/2008jcli2624.1

Linkin, M. E., & Nigam, S. (2008). The North Pacific Oscillation–West Pacific Teleconnection Pattern: Mature-Phase Structure and Winter Impacts. *Journal of Climate, 21*(9), 1979-1997. doi:10.1175/2007jcli2048.1

Meinen, C. S., & McPhaden, M. J. (2000). Observations of warm water volume changes in the equatorial Pacific and their relationship to El Niño and La Niña. *J Journal of Climate, 13*(20), 3551-3559.

Meinen, C. S., & McPhaden, M. J. (2001). Interannual variability in warm water volume transports in the equatorial Pacific during 1993–99. *Journal of Physical Oceanography, 31*(5), 1324-1345.

Rayner, N., Brohan, P., Parker, D., Folland, C., Kennedy, J., Vanicek, M., . . . Tett, S. (2006). Improved analyses of changes and uncertainties in sea surface temperature measured in situ since the mid-nineteenth century: The HadSST2 dataset. *Journal of Climate, 19*(3), 446-469.

Rogers, J. C. (1981). The north Pacific oscillation. *Journal of Climatology, 1*(1), 39-57.

Tseng, Y.-H., Ding, R., & Huang, X.-m. (2017). The warm Blob in the northeast Pacific—the bridge leading to the 2015/16 El Niño. *Environmental Research Letters, 12*(5). doi:10.1088/1748-9326/aa67c3

Vimont, D. J., Alexander, M., & Fontaine, A. (2009). Midlatitude Excitation of Tropical Variability in the Pacific: The Role of Thermodynamic Coupling and Seasonality. *Journal of Climate, 22*(3), 518-534. doi:10.1175/2008jcli2220.1

Vimont, D. J., Battisti, D. S., & Hirst, A. C. (2001). Footprinting: A seasonal connection between the tropics and mid-latitudes. *Geophysical Research Letters, 28*(20), 3923-3926. doi:10.1029/2001gl013435

Vimont, D. J., Wallace, J. M., & Battisti, D. S. (2003). The seasonal footprinting mechanism in the Pacific: Implications for ENSO. *Journal of Climate, 16*(16), 2668-2675. doi:Doi 10.1175/1520-0442(2003)016<2668:Tsfmit>2.0.Co;2

doi:10.6342/NTU202000712

White, W. B., Tourre, Y. M., Barlow, M., & Dettinger, M. (2003). A delayed action oscillator shared by biennial, interannual, and decadal signals in the Pacific Basin. *Journal of Geophysical Research, 108*(C3). doi:10.1029/2002jc001490

Yeh, S. W., Kug, J. S., Dewitte, B., Kwon, M. H., Kirtman, B. P., & Jin, F. F. (2009). El Nino in a changing climate. *Nature, 461*(7263), 511-514. doi:10.1038/nature08316

You, Y., & Furtado, J. C. (2017). The role of South Pacific atmospheric variability in the development of different types of ENSO. *Geophysical Research Letters, 44*(14), 7438-7446. doi:10.1002/2017gl073475

Yu, J.-Y., & Kim, S. T. (2011). Relationships between Extratropical Sea Level Pressure Variations and the Central Pacific and Eastern Pacific Types of ENSO. *Journal of Climate, 24*(3), 708-720. doi:10.1175/2010jcli3688.1

doi:10.6342/NTU202000712

FIGURE

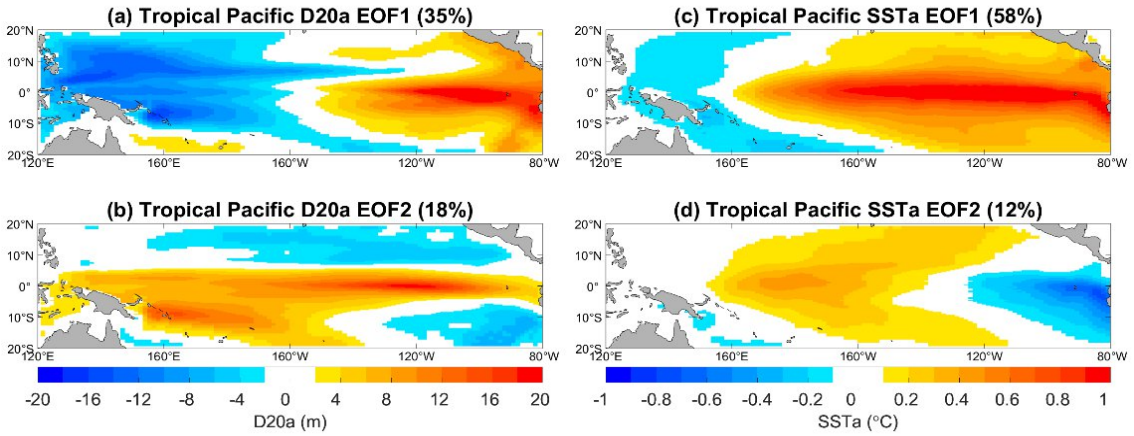

Figure 1. (a, b) The first and second EOF modes of monthly tropical Pacific D20a (shading, m). (c, d) Same as (a,b) but for SSTa (shading, ℃).

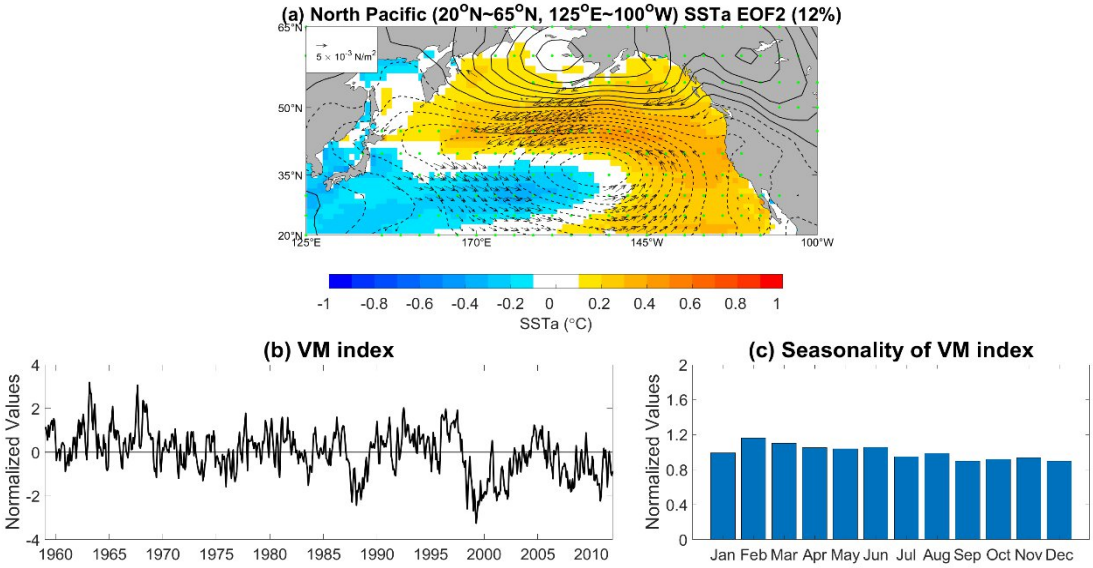

Figure 2. (a) The second EOF mode of monthly North Pacific SSTa (The Victoria mode) (shading, ℃). The regression of SLPa (contours, hPa) and wind stress anomalies onto the VM index is superimposed. The contour interval is 0.1 hPa. The shown wind vectors and the green dots (SLPa) are significant at the 95% confidence level. (b) The standardized VM index. (c) The standardized seasonality of the VM index.

doi:10.6342/NTU202000712

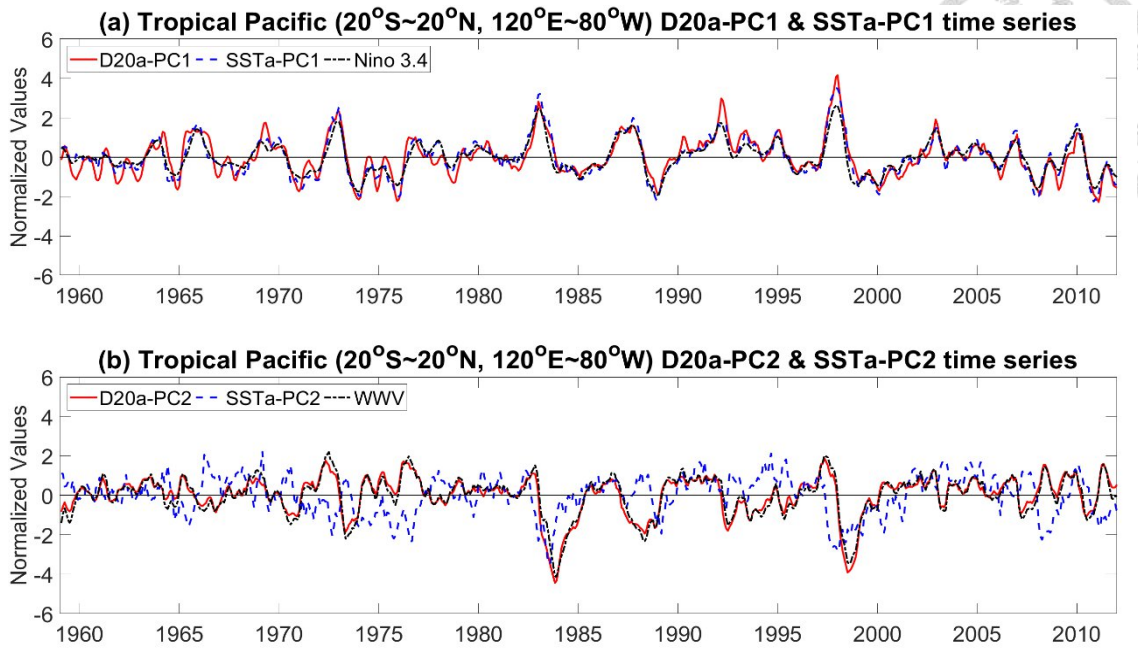

Figure 3. (a) Normalized PC1 time series of the tropical D20a and SSTa (Niño 3.4 index is superimposed). (b) Normalized PC2 time series of the tropical D20a and SSTa (WWV index is superimposed).

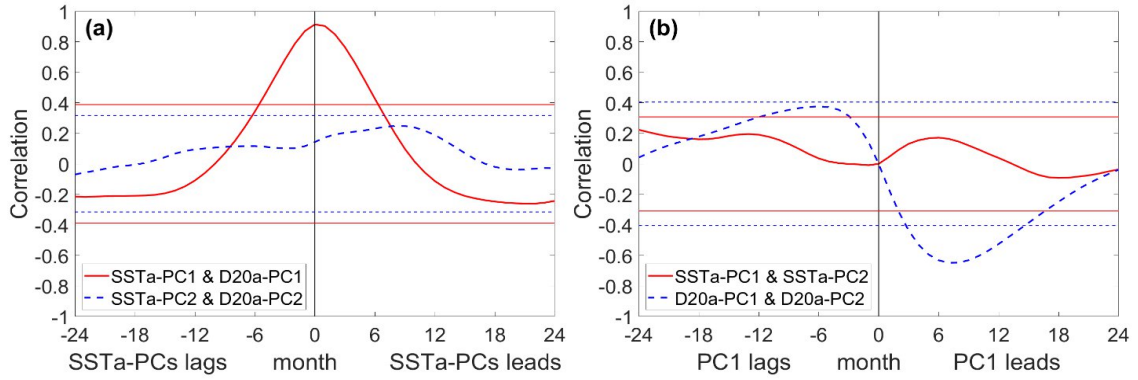

Figure 4. (a) The cross-correlation between the PCs of tropical SSTa and D20a. (b) The cross-correlations between the PC1 and PC2 of SSTa and D20a. The horizontal dashed and solid lines indicate the values exceed a 95% confidence level.

doi:10.6342/NTU202000712

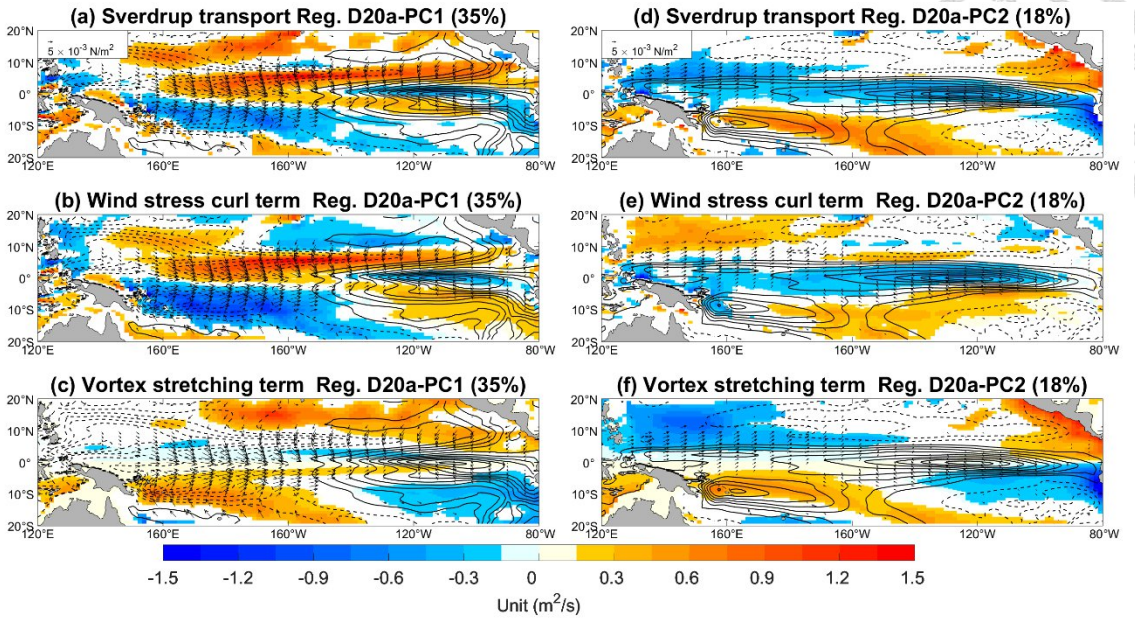

Figure 5. (a-c) Simultaneous regression map of Sverdrup transport (top panel), wind stress curl term (central panel) and vortex stretching (bottom panel) (Shading, m^2/s) onto the PC1 of tropical D20a. Simultaneous regressions of D20a (contours, m) and wind stress (arrows, N/m^2) onto the PC1 of tropical D20a are also superimposed. The contour interval is 2 m. (d-f) Same as (a-c) but for the PC2 of tropical D20a. The wind vectors shown are significant at the 95% level.

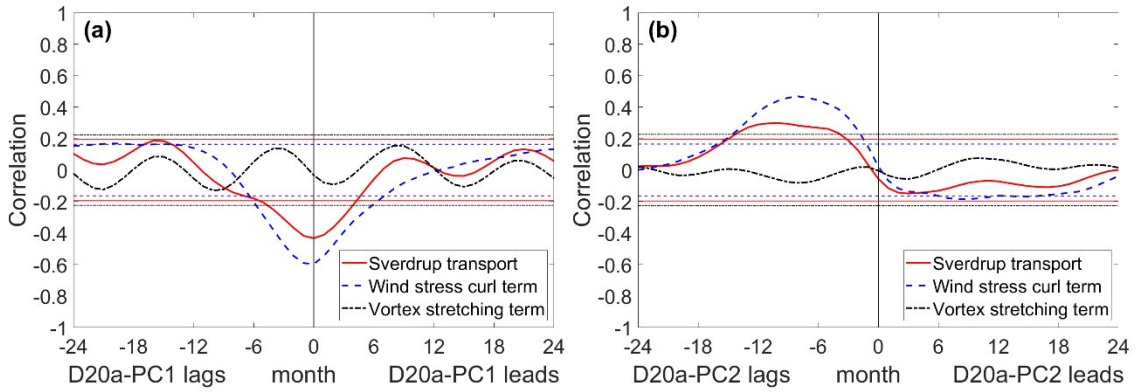

Figure 6. (a) The cross-correlation of Sverdrup transport and its related terms with the PC1 of tropical D20a. (b) Same as in (a) but for the PC2 of tropical D20a. The significant level of horizontal dashed and solid lines are the same as Figure 4.

doi:10.6342/NTU202000712

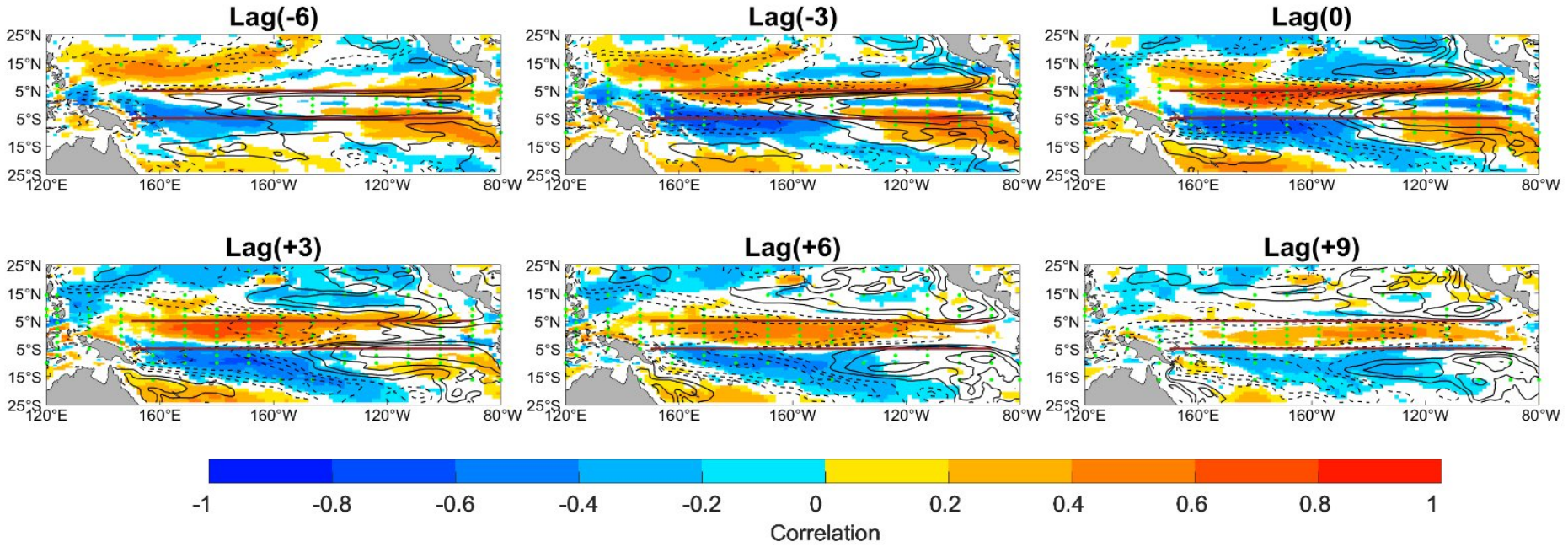

Figure 7. The correlation map of wind stress curl term (contributing to Sverdrup transport) (shading) and D20a (contours) onto the PC1 of D20a at different lags. Contour levels are 0.2. The shading and green dots are significant at a 95% confidence level. 5°N and 5°S latitudes are highlighted brown.

doi:10.6342/NTU202000712

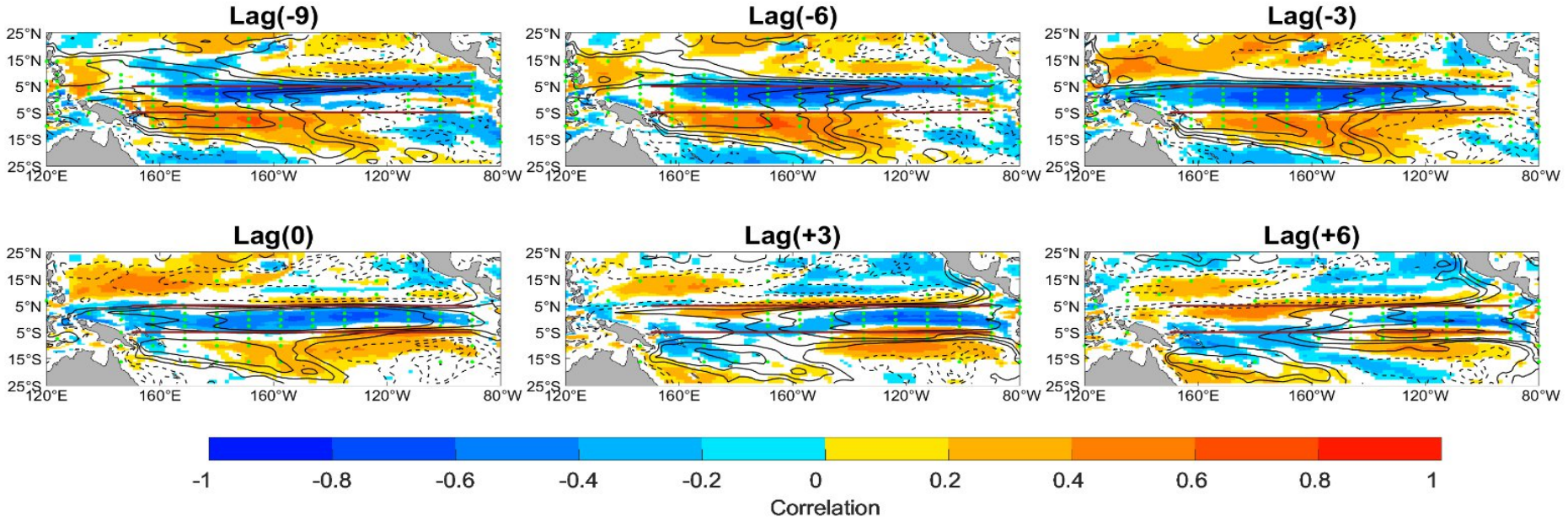

Figure 8. Same as Figure 7 but for the PC2 of D20a.

doi:10.6342/NTU202000712

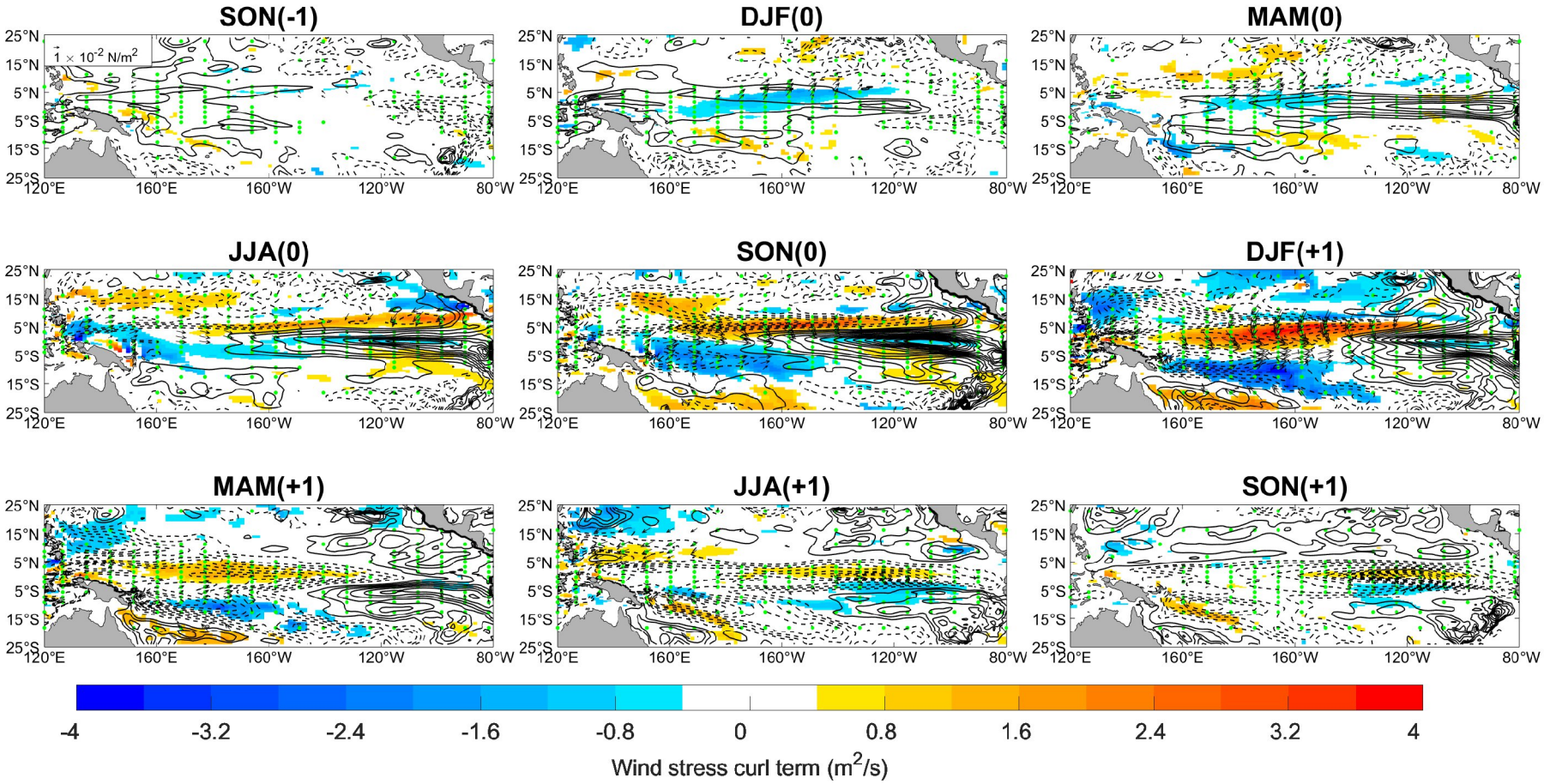

Figure 9. The Sverdrup transport driven by wind stress curl term (shading, m^2/s) composite of the PC1 of D20a. The corresponding D20a (contours, m) and wind stress anomalies are superimposed. The contour interval is 3 m. The wind vectors and the green dots defined as D20a plotted only where significant at the 95% level.

doi:10.6342/NTU202000712

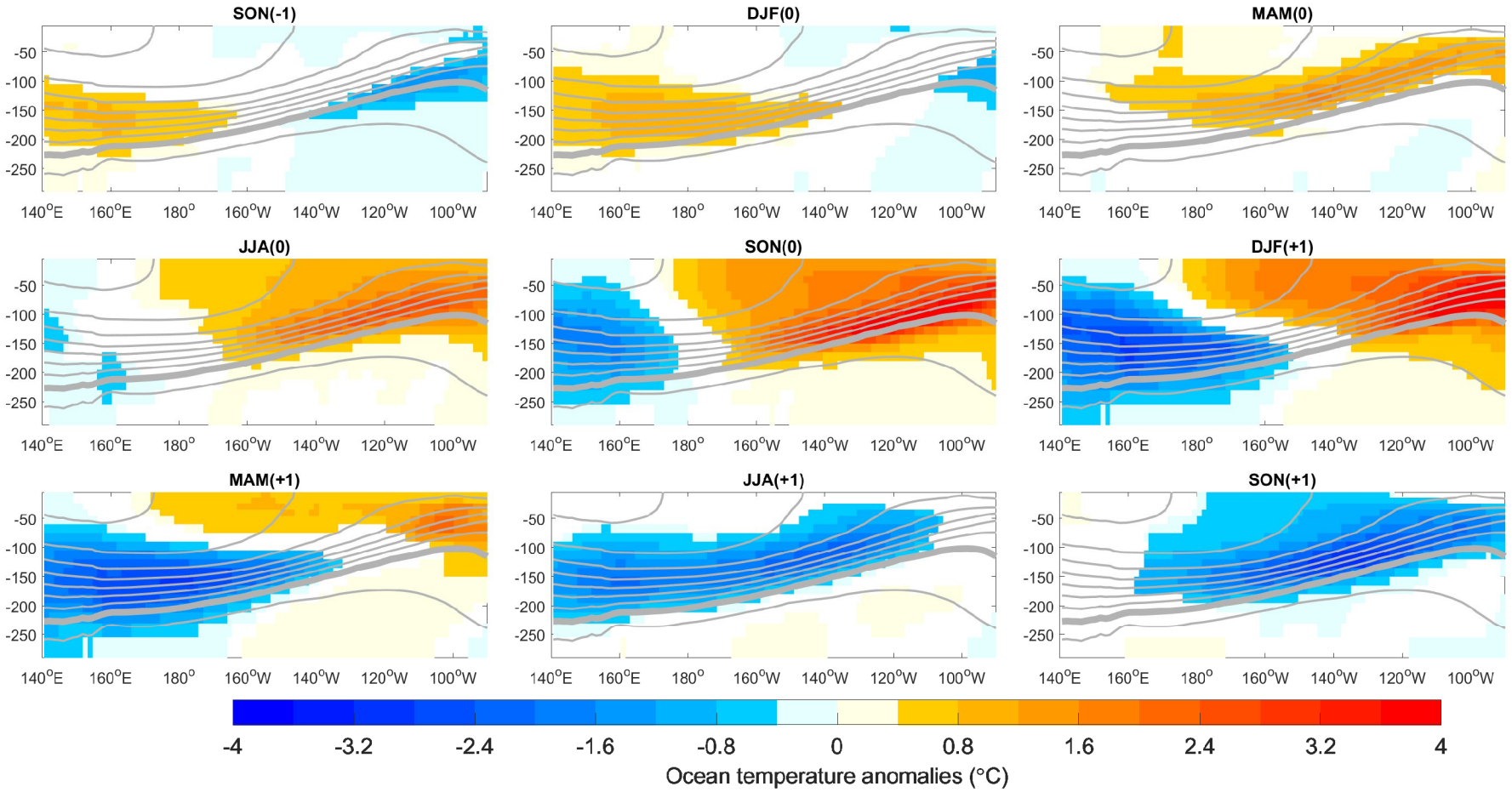

Figure 10. The subsurface temperature (shading, ℃) composite of the PC1 of D20a. Climatological isotherms are shown as contours (℃, the interval is 2℃). The thick gray line is 15℃ isotherm.

doi:10.6342/NTU202000712

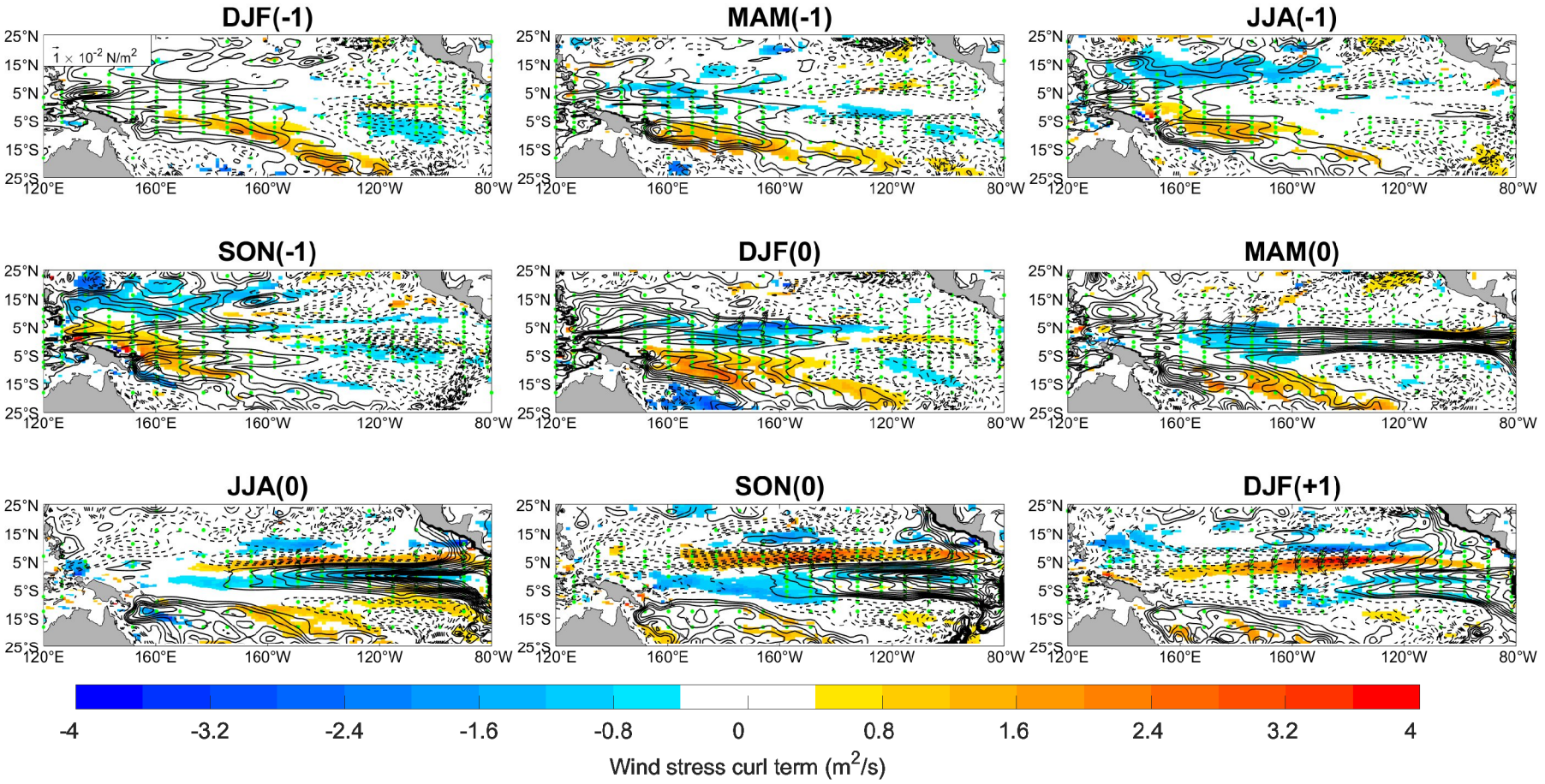

Figure 11. Same as Figure 9 but for the PC2 of D20a.

doi:10.6342/NTU202000712

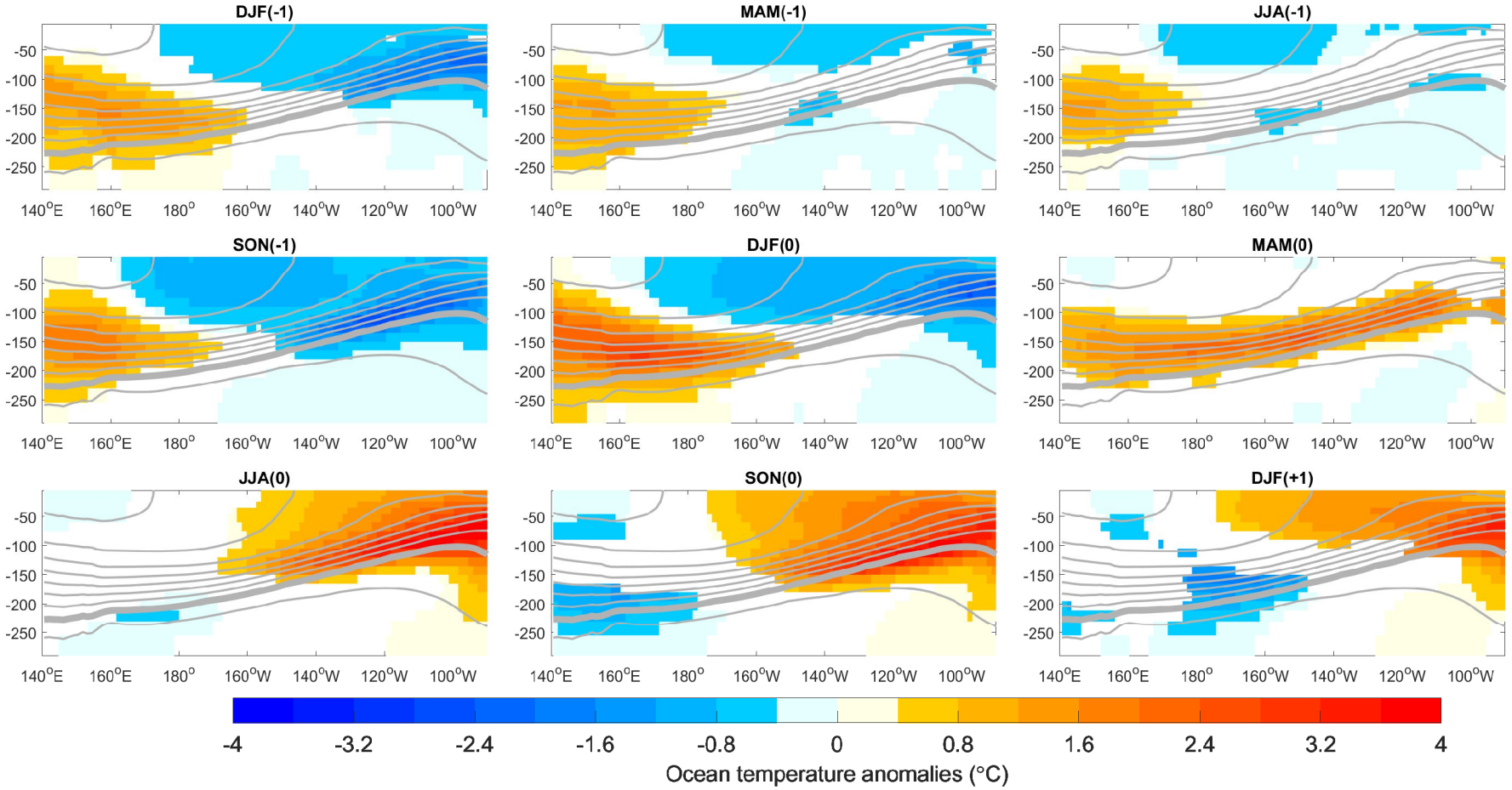

Figure 12. Same as Figure 10 but for the PC2 of D20a (basin mode).

doi:10.6342/NTU202000712

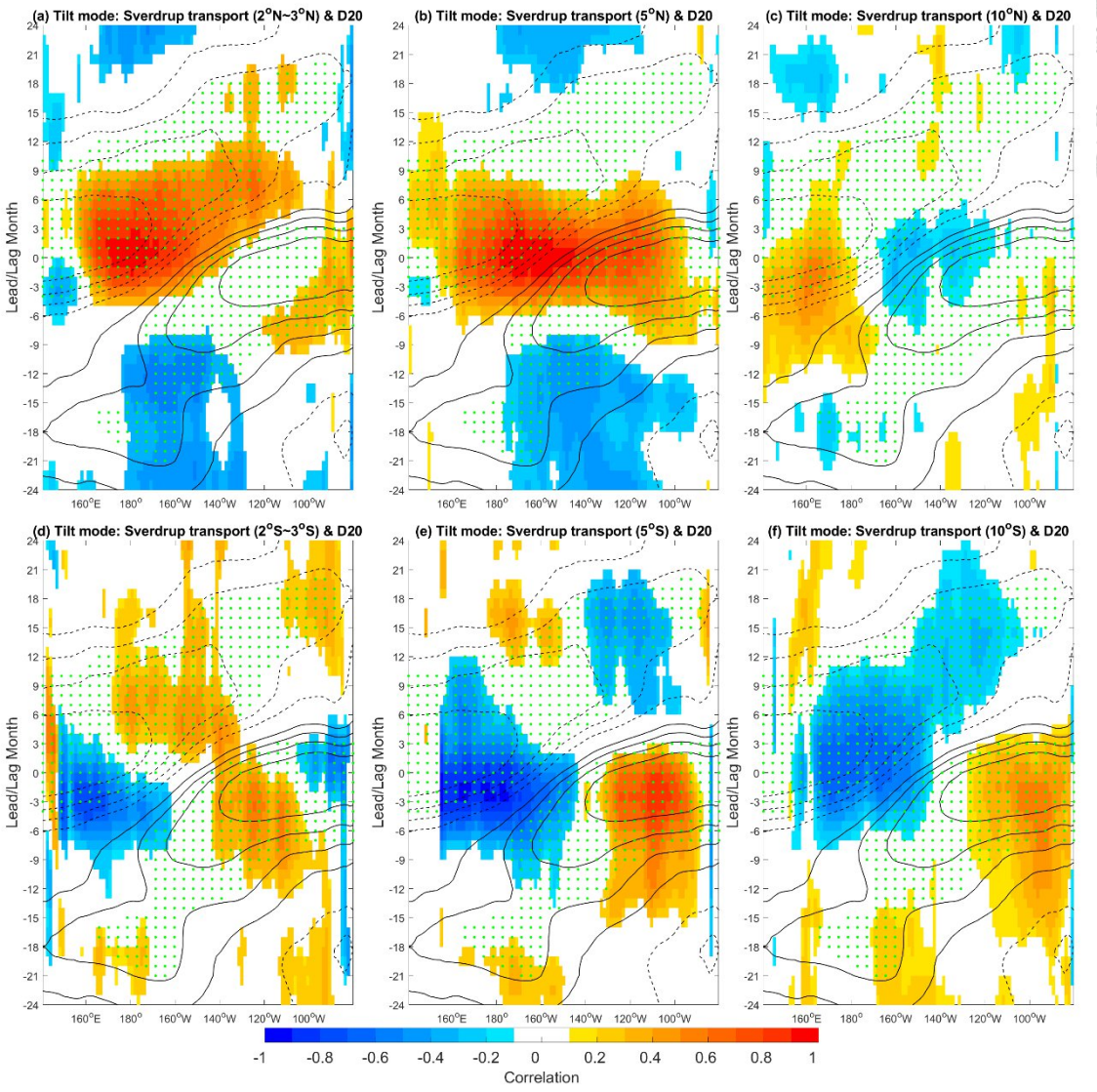

Figure 13. Lead-lag correlation of D20a (contours) and Sverdrup transport contributed by wind stress curl term (shading) averaged between (a) 2°N~3°N, (b) 5°N, (c) 10°N and (d) 2°S~3°S, (e) 5°S, (f) 10°S with the PC1 of D20a (tilt mode). Positive correlations of Sverdrup transport represent longitudes and times with convergence of mass transport near the equator. The contours interval is 0.2. Significance at the 95% level is labeled by green dots.

doi:10.6342/NTU202000712

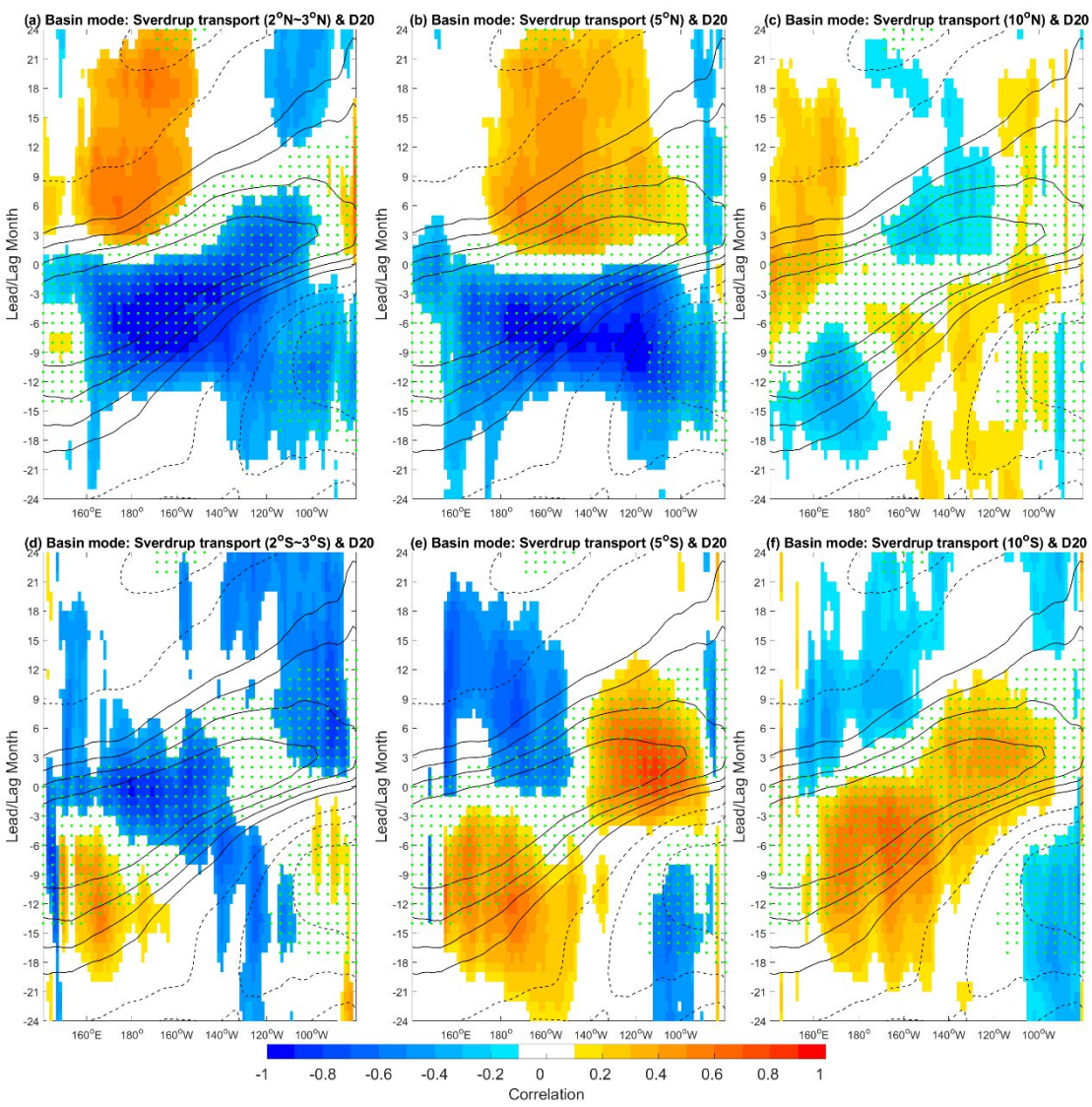

Figure 14. Same as Figure 13 but for the PC2 of D20a (basin mode).

doi:10.6342/NTU202000712

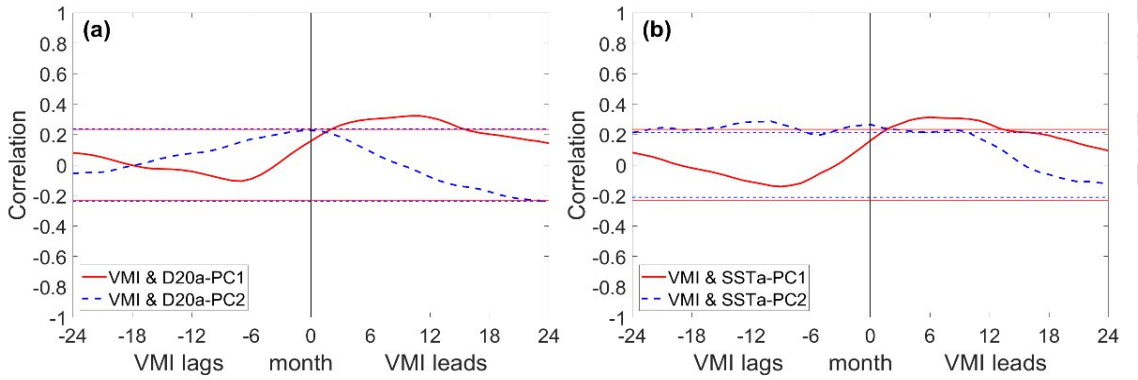

Figure 15. (a) The cross-correlation of the VM index (VMI) with the two leading PCs of D20a. (b) Same as (a) but for SSTa. The horizontal dashed and solid lines indicate the values exceed a 95% confidence level.

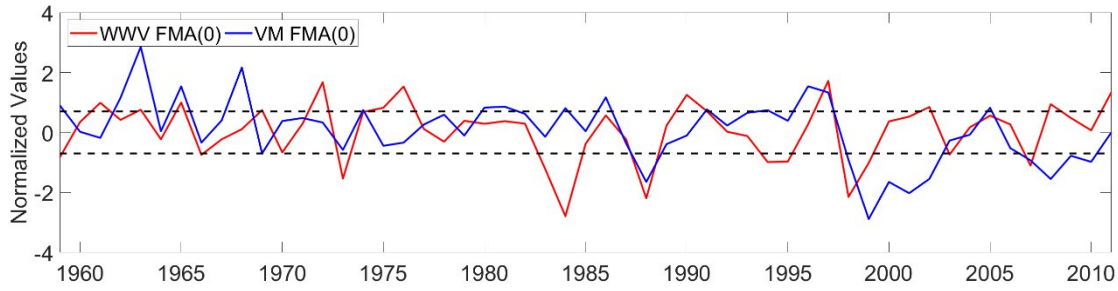

Figure 16. The time series of the FMA VM and WWV indices. The horizontal dashed line indicates ± 0.7 standard deviations.

doi:10.6342/NTU202000712

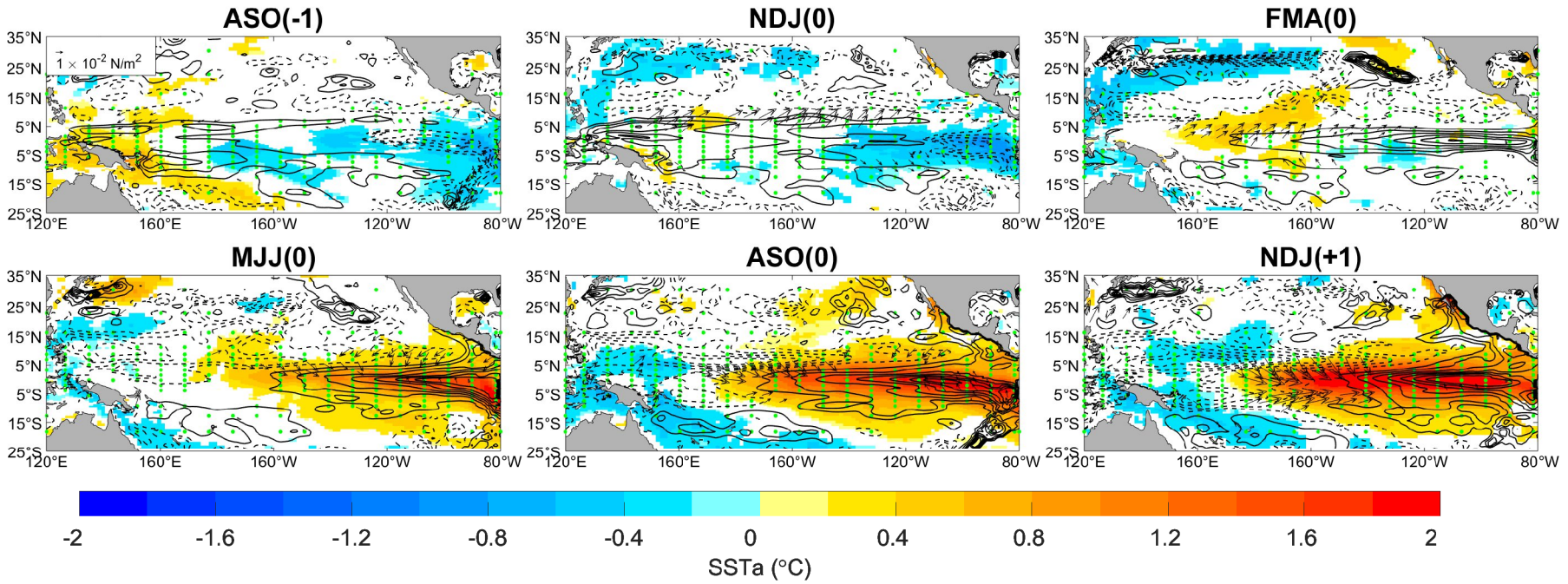

Figure 17. The SSTa (shading, ℃) composite of positive VM and positive WWV years. The corresponding D20a (contours, m) and wind stress anomalies are superimposed. The contour interval is 5 m. The wind vectors and the green dots defined as D20a plotted only where significant at the 95% level.

doi:10.6342/NTU202000712

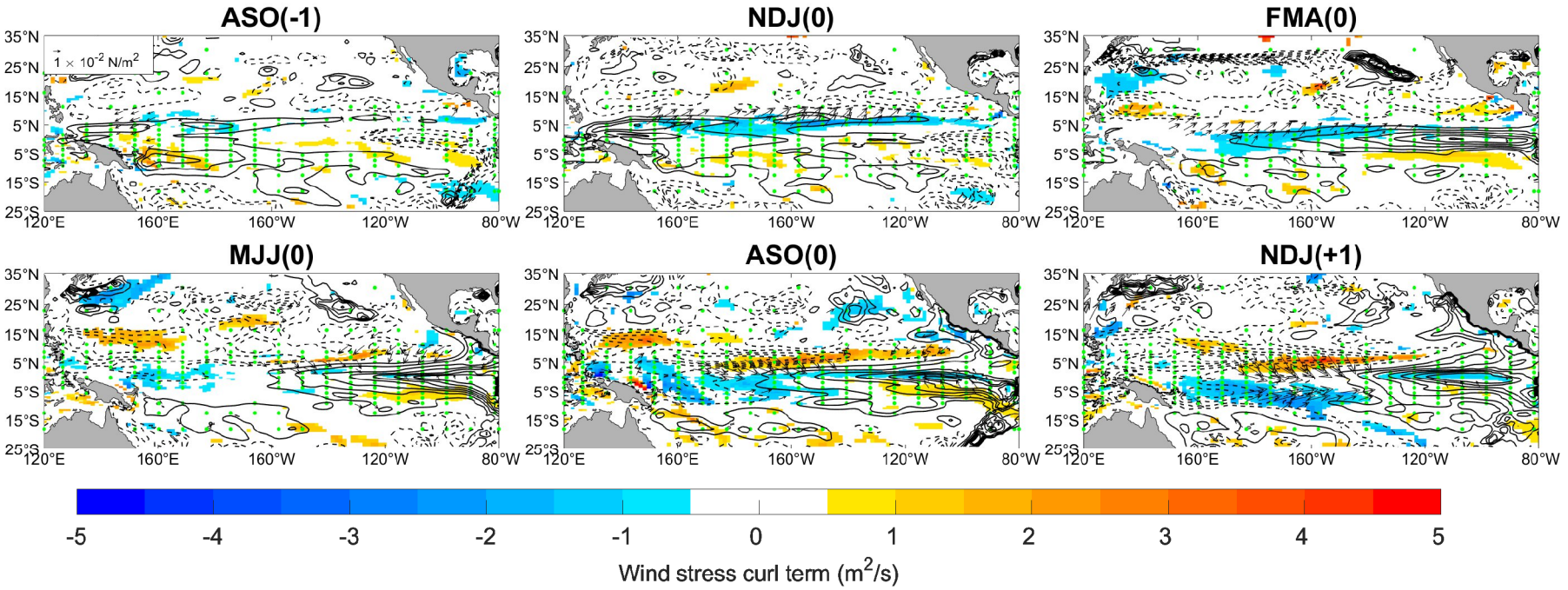

Figure 18. Same as Figure 17 but replace the shading by the Sverdrup transport contributed by wind stress curl term (shading, m^2/s).

doi:10.6342/NTU202000712

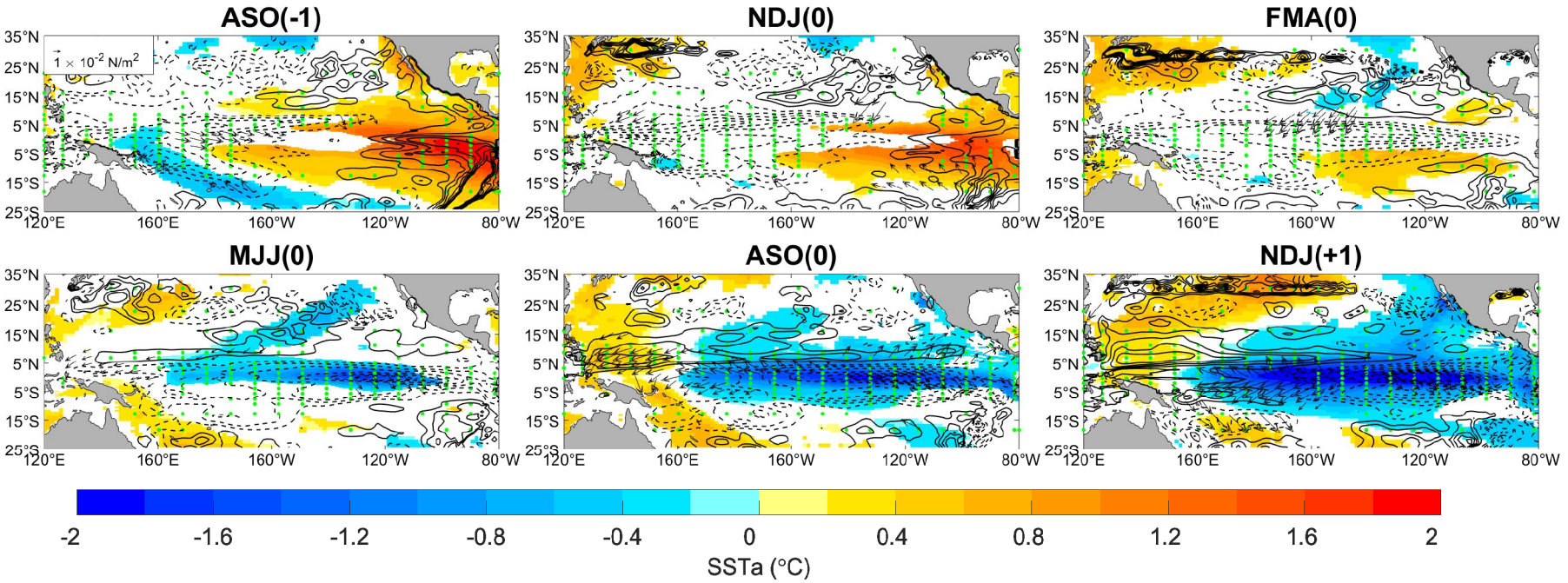

Figure 19. Same as Figure 17 but for the negative VM and negative WWV years.

doi:10.6342/NTU202000712

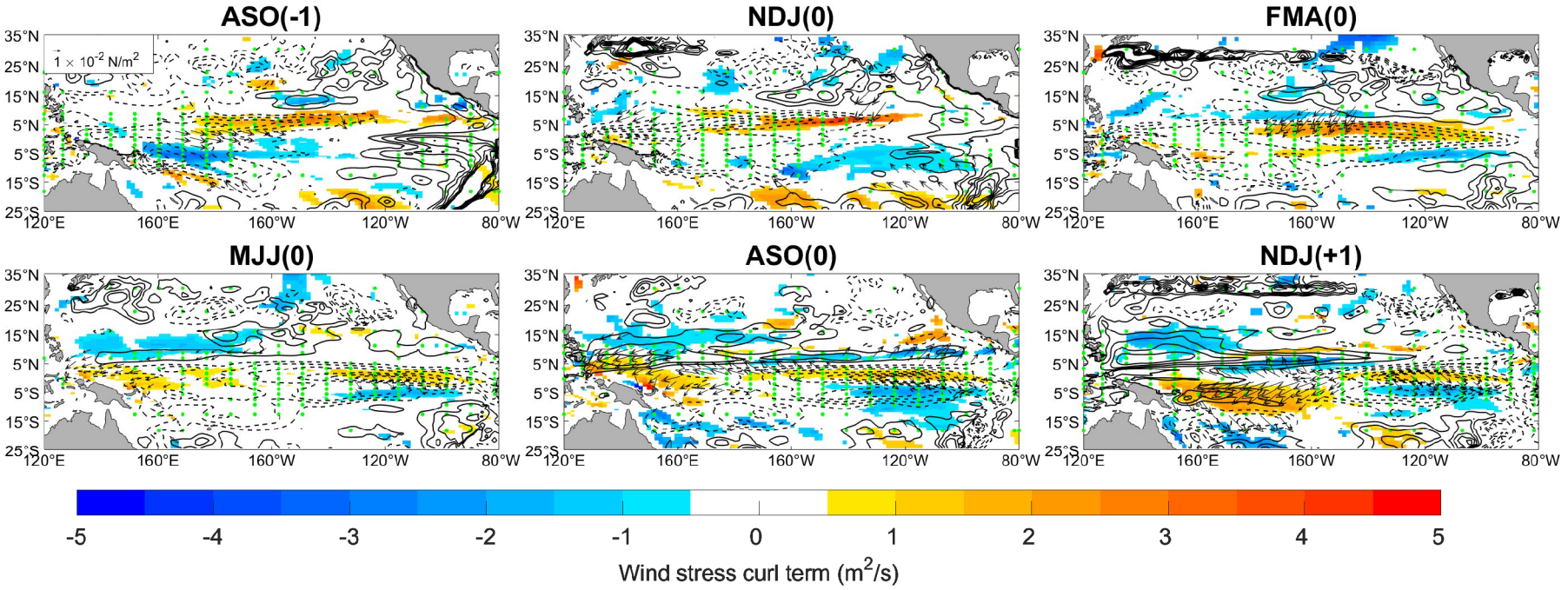

Figure 20. Same as Figure 19 but replace the shading by the Sverdrup transport contributed by wind stress curl term (shading, m^2/s).

doi:10.6342/NTU202000712

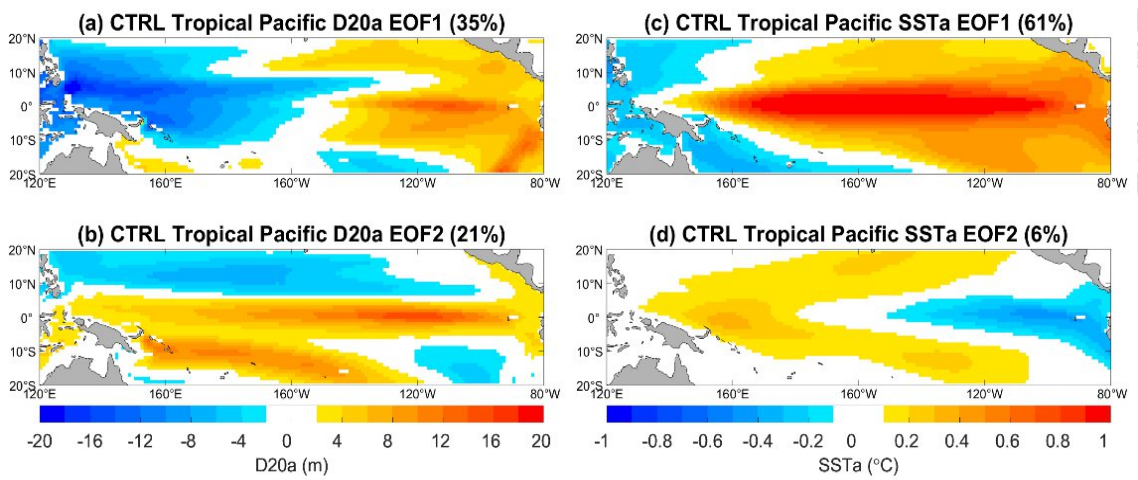

Figure 21. (a, b) The first and second EOF modes of monthly tropical Pacific D20a (shading, m) in the CTRL run. (c, d) Same as (a, b) but for the SSTa (shading, ℃).

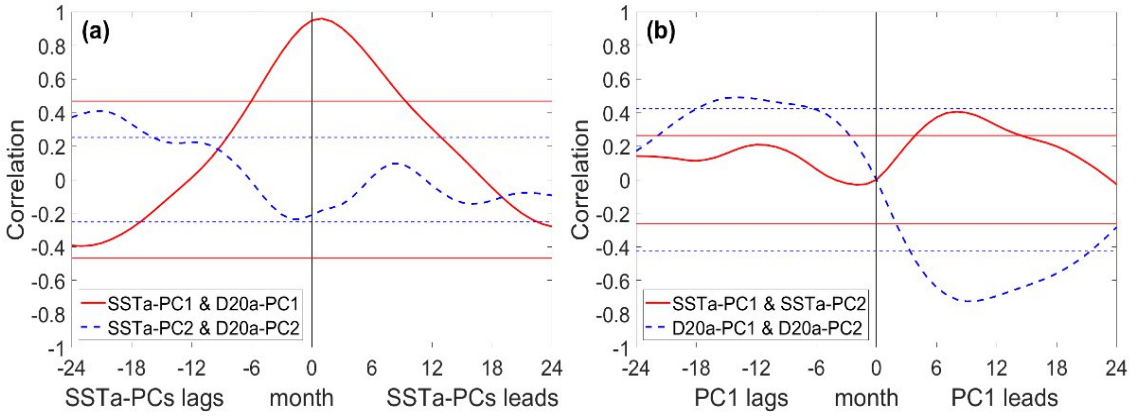

Figure 22. (a) The cross-correlation between the PCs of tropical SSTa and D20a in the CTRL run. (b) The cross-correlation between the PC1 and PC2 of SSTa and D20a in the CTRL run. The horizontal dashed and solid lines indicate the values exceed a 95% confidence level.

doi:10.6342/NTU202000712

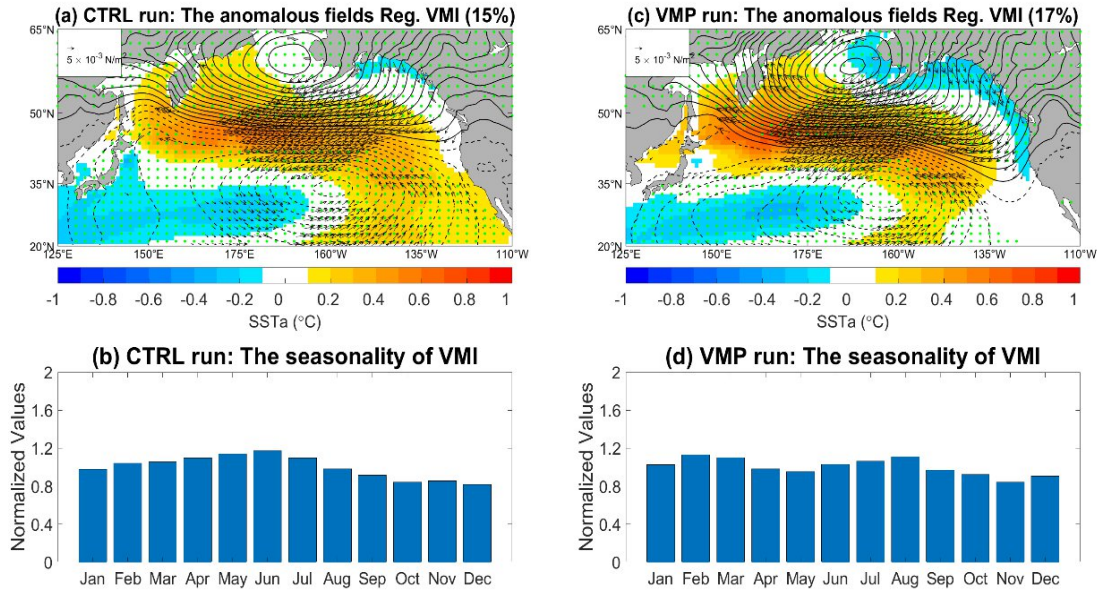

Figure 23. (a) The second EOF mode of monthly North Pacific SSTa (The Victoria mode) (shading, ℃) in the CTRL run. The regression of SLPa (contours, hPa) and wind stress anomalies onto the VM index is superimposed. The shown wind vectors and the green dots (SLPa) are significant at the 95% confidence level. (b) The standardized seasonality of the VM index in the CESM CTRL run. (c, d) Same as (a, b) but for the VMP run.

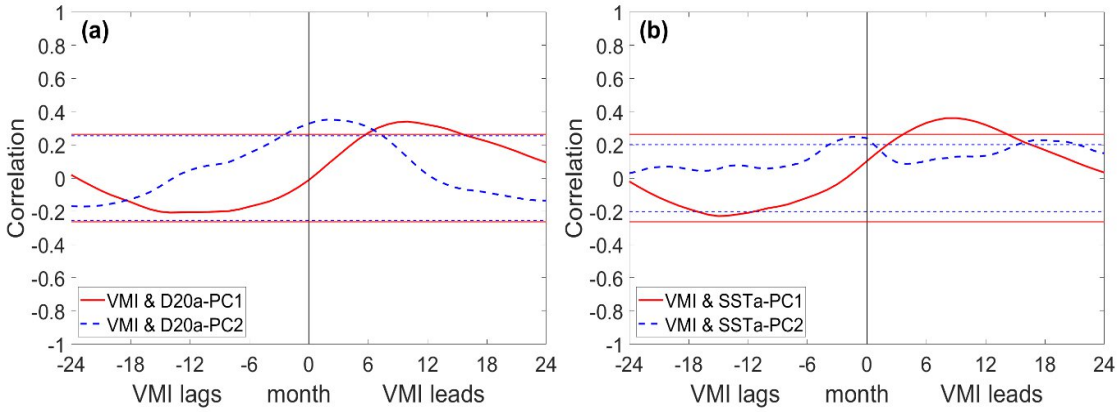

Figure 24. Same as Figure 4 but for the CTRL run.

doi:10.6342/NTU202000712

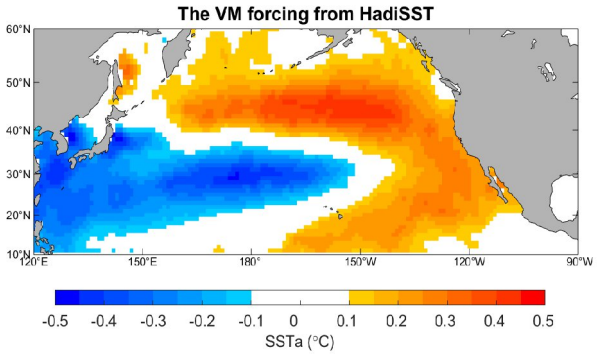

Figure 25. The SSTa pattern associated with VM forcing (shading, ℃), calculated by the regression of SSTa onto the FMA-averaged VM index from the HadiSST data.

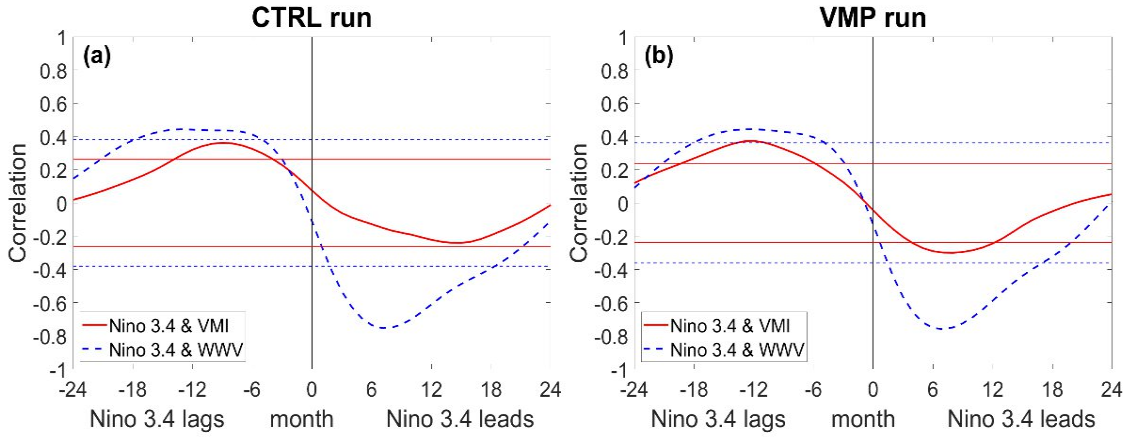

Figure 26. (a) The cross-correlation of the Niño 3.4 index with the VM and WWV indices in the CTRL run. (b) Same as (a) but for the VMP run. The horizontal dashed and solid lines indicate the values exceed a 95% confidence level.

doi:10.6342/NTU202000712

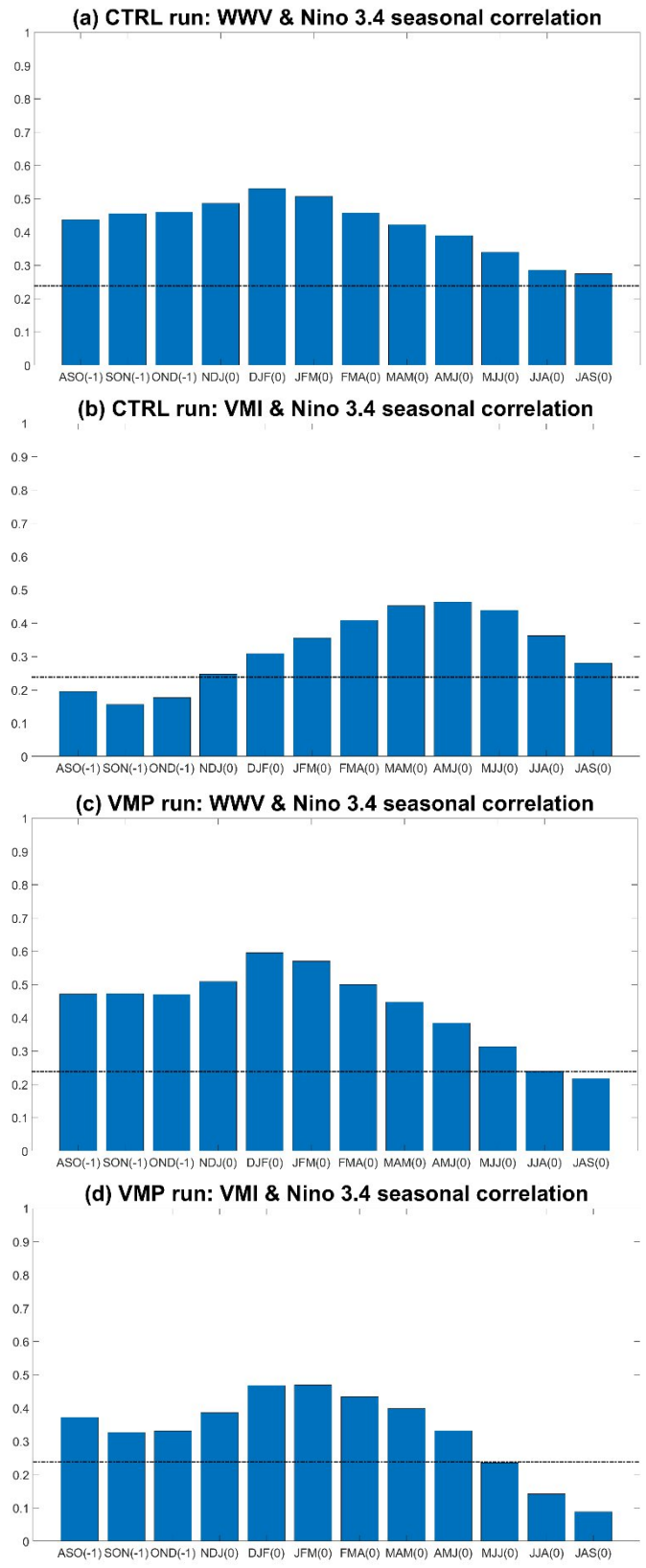

Figure 27. The seasonal correlations of the WWV and VM indices in different seasons with DJF (+1) Niño 3.4 index for (a, b) CTRL run and (c, d) VMP run. The horizontal lines indicate the values exceed a 95% confidence level.

doi:10.6342/NTU202000712

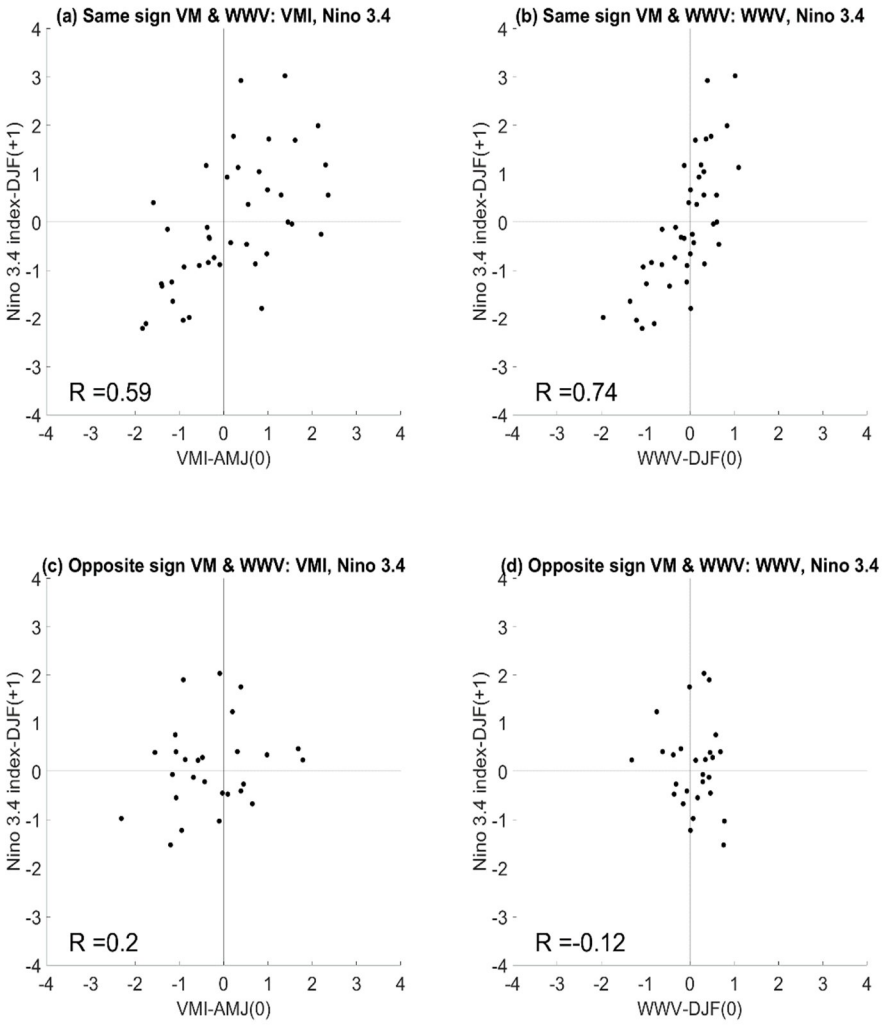

Figure 28. (a, b) the scatterplots of AMJ (0) VMI and DJF (0) WWV versus subsequent DJF (+1) Niño 3.4 index for same sign of VM and WWV indices in the CTRL run. (c, d) The scatterplots of AMJ (0) VMI and DJF (0) WWV versus subsequent DJF (+1) Niño 3.4 index for the opposite sign of VM and WWV indices. Correlation coefficients are presented in each panel and correlations of same sign case are significant at 95% confidence level while correlations of the opposite sign are not significant.

doi:10.6342/NTU202000712

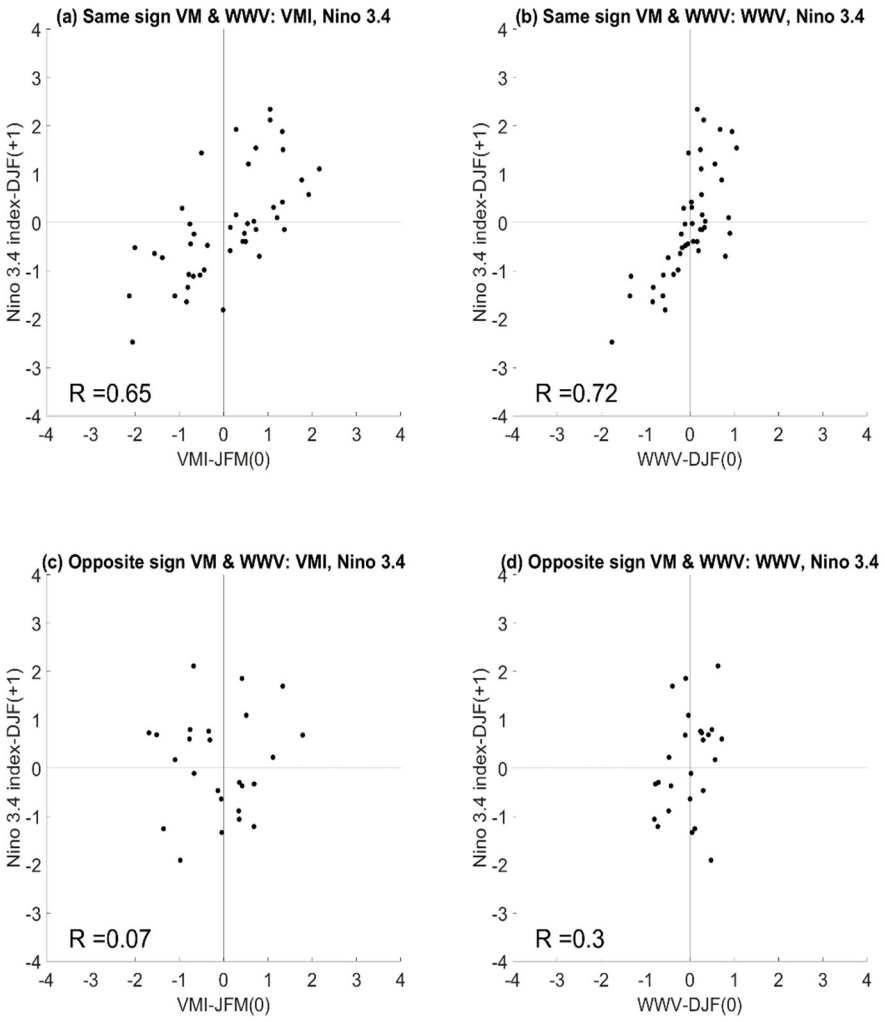

Figure 29. Same as Figure 28 but for the VMP run.

doi:10.6342/NTU202000712

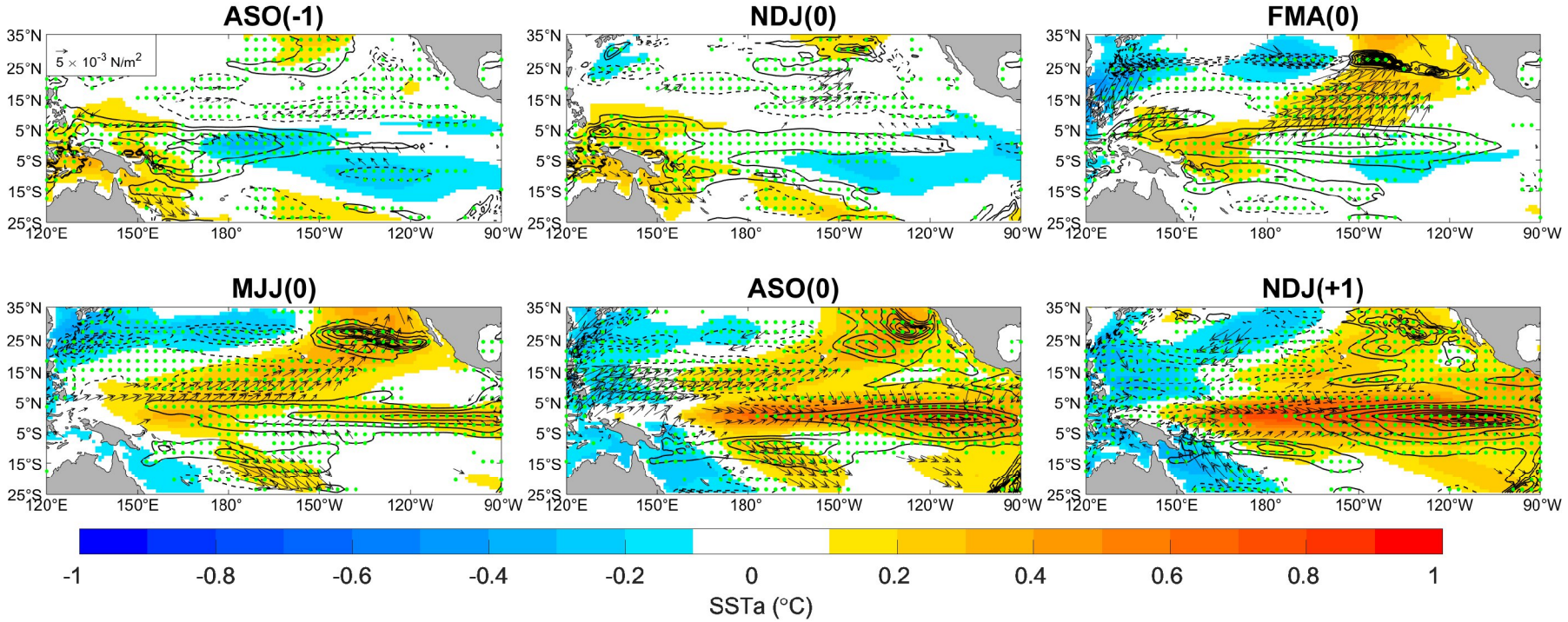

Figure 30. Same as Figure 17 but for the CTRL run.

doi:10.6342/NTU202000712

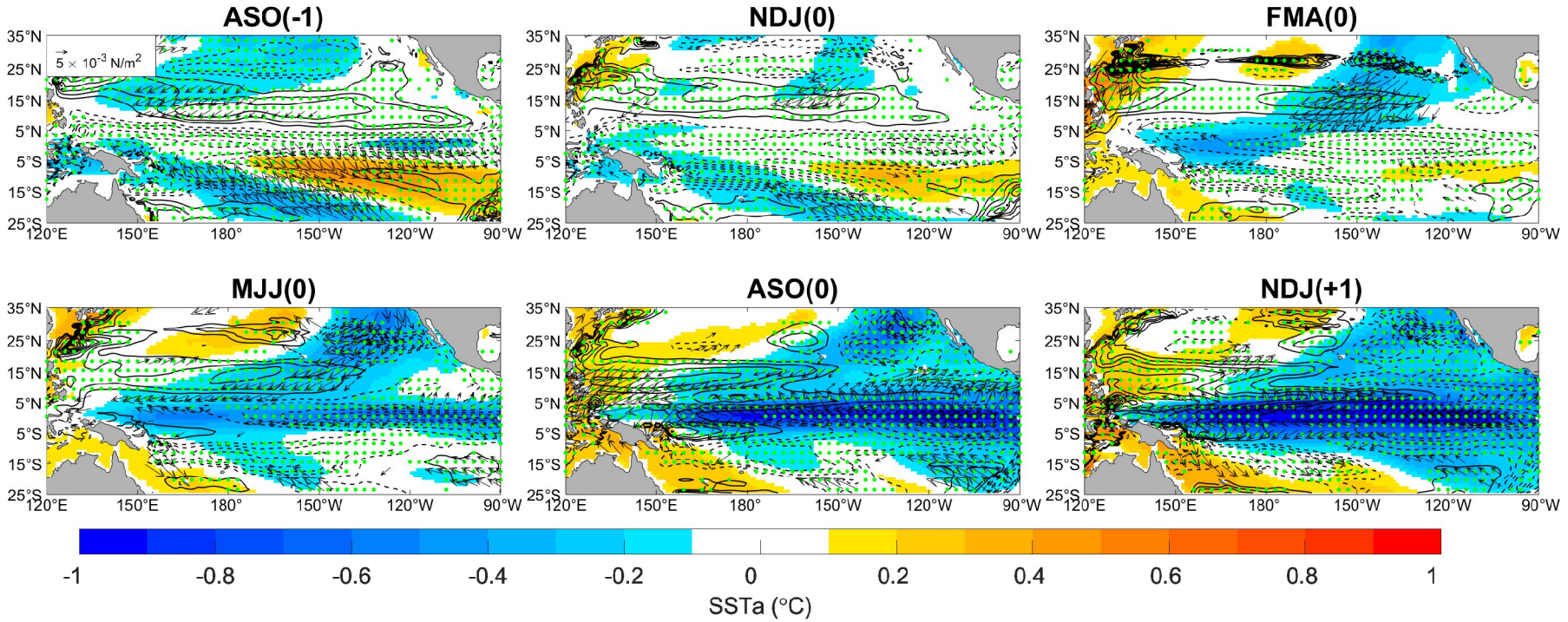

Figure 31. Same as Figure 19 but for the CTRL run.

doi:10.6342/NTU202000712

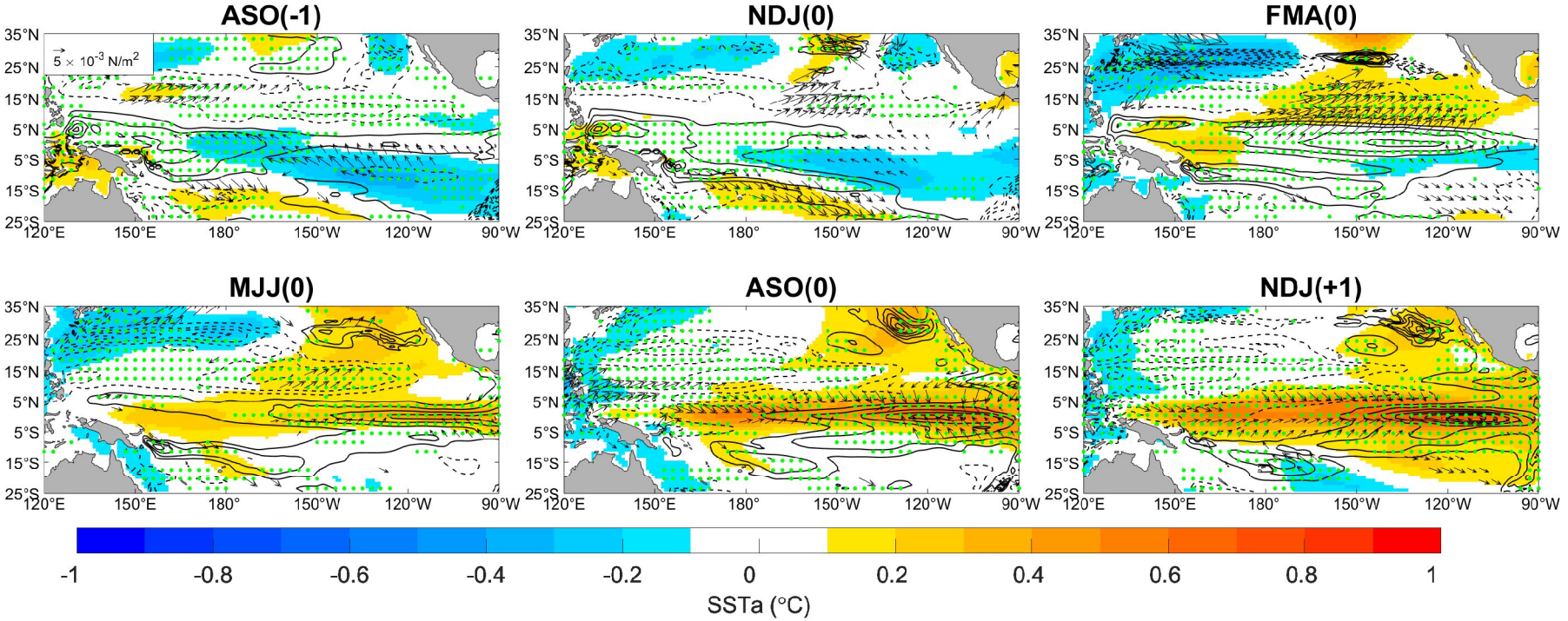

Figure 32. Same as Figure 17 but for the VMP run.

doi:10.6342/NTU202000712

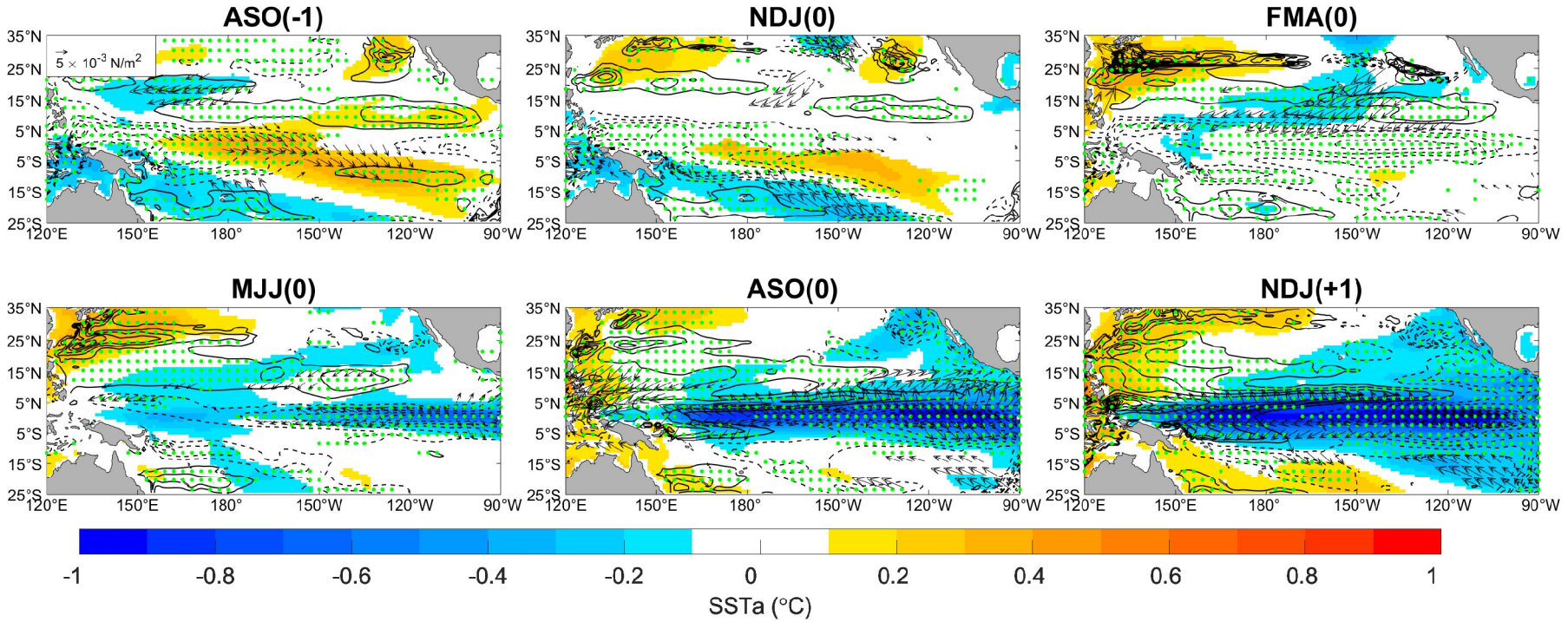

Figure 33. Same as Figure 19 but for the VMP run.

doi:10.6342/NTU202000712

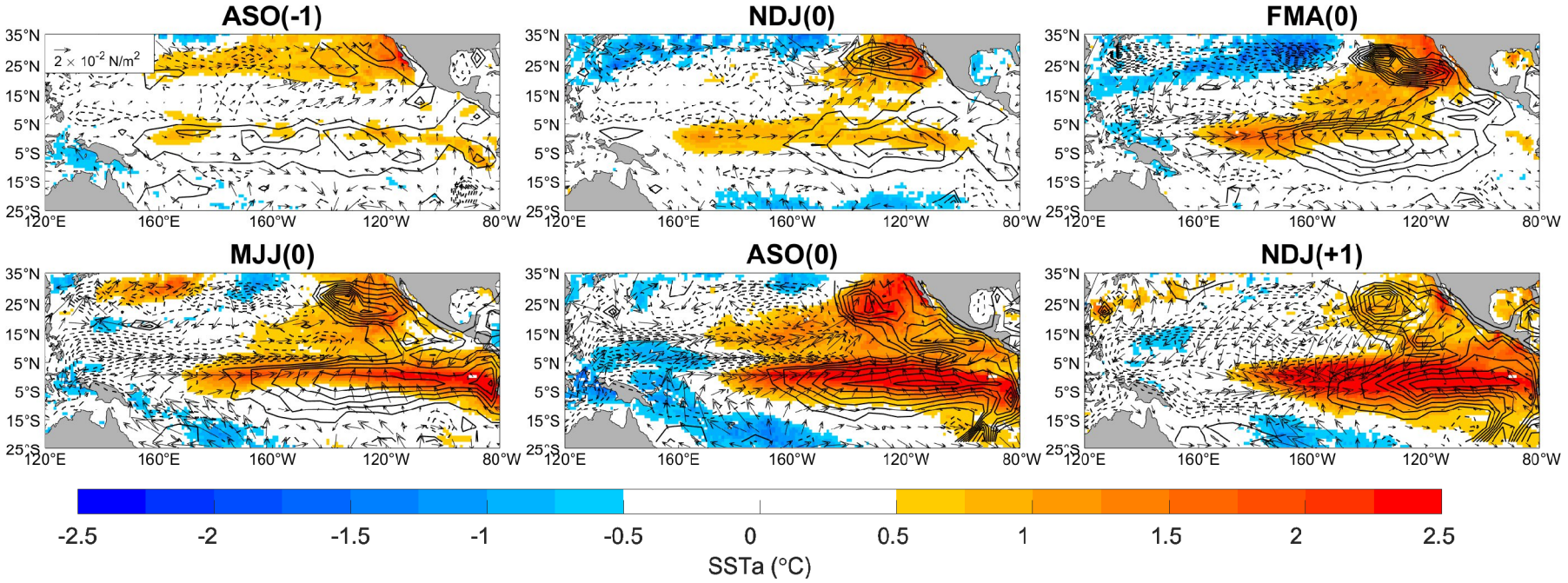

Figure 34. Same as Figure 17 but for the El Niño year in 2015-16. Observation data is from the ECMWF ocean reanalysis system 5 (ORAS5).

doi:10.6342/NTU202000712

TABLE

	Positive WWV events	Negative WWV events
Positive VM events	1963-64 1965-66 1991-92 1997-98	1984-85 1994-95
Negative VM events	1969-70 2002-03 2008-09	1988-89 1998-99 1999-00 2007-08

Table 1. The classification of years in which positive or negative VM and WWV events are following by an El Niño (in red) or La Niña (in blue) event for the period 1959~2011.

doi:10.6342/NTU202000712